Over a ten-year record of aerosol optical properties at SMEAR II

Krista Luoma[1], Aki Virkkula[1,2], Pasi Aalto[1], Tuukka Petäjä[1] and Markku Kulmala[1]

[1]Institute for Atmospheric and Earth System Research, University of Helsinki, Helsinki, 00014, Finland
[2]Finnish Meteorological Institute, Helsinki, 00560, Finland

Correspondence to: Krista Luoma (krista.q.luoma@helsinki.fi), Aki Virkkula (aki.virkkula@fmi.fi)

Abstract. The aerosol optical properties (AOPs) describe the ability of aerosols to scatter and absorb radiation at different wavelengths. Since the aerosol particles interact with the radiation from the sun, they also have an impact on the climate. Our study focuses on the long-term trends and seasonal variations of different AOPs measured at a rural background station in Northern Europe. To explain the observed variations in the AOPs, we also analyzed changes in the aerosol size distribution. AOPs of particles smaller than 10 µm (PM10) and 1 µm (PM1) have been measured at SMEAR II, in Southern Finland, since 2006 and 2010, respectively. For the PM10 particles the mean values of the scattering and absorption coefficients, single-scattering albedo, and backscatter fraction at λ = 550 nm were 15.2 Mm^{-1}, 2.1 Mm^{-1}, 0.87 and 0.14. The scattering and absorption Ångström exponents at the wavelength ranges 450–700 nm and 370–950 nm were 1.80 and 0.95, respectively. Statistically significant trends were found for example for the PM10 scattering and absorption coefficients, single-scattering albedo, and backscatter fraction, and the slopes of these trends were -0.32 Mm^{-1}, -0.086 Mm^{-1}, $2.2 \cdot 10^{-3}$, and $1.3 \cdot 10^{-3}$ per year. The tendency for the extensive AOPs to decrease correlated well with the decrease in aerosol number and volume concentration. The tendency for the single-scattering albedo and backscattering fraction to increase indicates that the aerosol size distribution consist of less larger particles and that aerosols absorb relatively less light than before. The trends of the single-scattering albedo and backscattering fraction influenced the effective aerosol forcing efficiency, indicating that the aerosol particles are scattering the radiation more effectively back into space.

1 Introduction

Aerosol particles directly affect the climate by scattering and absorbing the shortwave radiation from the sun (ARI, *aerosol–radiation interaction*) (Charlson et al., 1992). Aerosol particles can either have a warming or cooling effect on the climate, depending on the optical properties of the aerosol particles and the surface below the aerosol layer. ~~The ARI is dependent on the reflectivity of the aerosol particles as well as on the albedo of the surface below the aerosol layer. For the aerosol particles to have a cooling (warming) effect, the reflectivity of the particles must be higher (lower) than the albedo of the surface (Haywood and Shine, 1995).~~ Aerosol particles also affect the climate via aerosol–cloud interactions (ACIs) since aerosol particles may act as cloud condensation nuclei (CCN). By functioning as CCN, aerosol particles also affect the optical properties of the cloud (Haywood and Boucher, 2000). The more CCN are available, the smaller and more numerous are the cloud droplets. Clouds with more droplets scatter light more efficiently, so they have a larger cooling effect than clouds that

have fewer droplets (Twomey, 1991). Clouds with smaller droplets have longer lifetimes, since it requires more time for the cloud droplets to grow to the size of rain drops (Lohmann and Feichter, 1997). Longer lifetimes also increase the cooling effect of the clouds.

There are vast uncertainties in determining the global radiative forcing related to aerosol particles (Boucher et al., 2013). The number concentration, chemical composition and size distribution of aerosol particles vary widely both spatially and temporally, so it is challenging to consider them in the models. Challenges arise even more with the ACIs that include highly complex processes.

The aerosol optical properties (AOPs) describe how much the particles scatter and absorb radiation at different wavelengths. It is essential to know how the aerosol particles interact with radiation to determine the direct effect on the climate. The extensive optical properties, such as scattering and absorption coefficients, are dependent on the mass and/or volume of the particles and also on their size distribution and chemical composition. Intensive properties, however, are not dependent on the amount of aerosol but on the properties of the particles, such as the size distribution and composition. Intensive properties ~~can be determined by comparing~~are calculated from the scattering, backscattering and absorption measurements at different wavelengths. Therefore, by measuring the AOPs at different wavelengths, we can also obtain indirect information on the size distribution and chemical composition of the aerosol particles. ~~This explains why the measurements of AOPs can give practical results.~~

In situ measurements of AOPs have been conducted at SMEAR II (Station for Measuring Ecosystem–Atmosphere Relations; Hari and Kulmala, 2005) in Hyytiälä, Finland since 2006. SMEAR II is located in the middle of a pine forest and represents the atmospheric conditions typically found in boreal forests (Hari et al., 2013). Boreal forests are sources for new aerosol particles that are formed in a gas-to-particle conversions (Kulmala et al., 2004; Kulmala et al., 2013). Boreal forests (also known as Taiga) cover approximately 30 % of the world's forests and 8 % of the earth's surface, so they greatly affect the global radiation budget.

The measurements of AOPs were started for aerosol particles smaller than 10 µm in diameter (PM10). The PM10 measurements are sensitive to coarse particles that are typically primary and originated from natural sources, such as soil dust and sea salt. To obtain additional information about submicron particles, parallel measurements of AOPs for PM1 were launched in June 2010. Motivation to measure also PM1 particles is that secondary aerosols (both natural and anthropogenic), and anthropogenic primary aerosols are typically submicron particles. Having measurements for different cut-offs makes the measurements also more comparable between different stations, since stations might use different cut-off sizes. To study the causalities between the AOPs and the size distribution, we have also included the measurements of aerosol size distribution to our study.

Here, we present the observed temporal variation and trends of the AOPs at SMEAR II. These AOPs have been previously discussed by Virkkula et al. (2011) and Pandolfi et al. (2018). Virkkula et al. (2011) used the integrating nephelometer and the aethalometer data from a 3-year period (2006–2009). Pandolfi et al. (2018) compared the aerosol scattering measurements that were conducted at different measurement sites in Europe. At SMEAR II, the study involved nephelometer data, from 2006 to 2015. However, these articles determined the AOPs of the PM10 particles only, and Pandolfi et al. (2018) did not include absorption data. Long time series (2006–2017) of the measurements of both scattering and absorption together at SMEAR II have not been presented before, nor have the optical properties of the PM1 particles.

2 Measurements and methods

2.1 The field site

The measurements presented here were conducted at the SMEAR II station in Hyytiälä, southern Finland (61° 51' N, 24° 17' E, 181 m above sea level.). SMEAR II is located in the middle of a forest that consists mostly of Scots pine (*Pinus sylvestris* L.) trees (Hari et al., 2013). The nearest larger cities, Tampere (220 000 inhabitants) and Jyväskylä (140 000 inhabitants), are located about 60 km and 100 km from the measurement station. Otherwise, the area is sparsely populated and there are no large pollution sources nearby the station.

2.2 Instrumentation

2.2.1 Measurements of aerosol optical properties

AOPs have been measured at SMEAR II since June 2006. The measurements of aerosol scattering, backscattering and absorption coefficients (σ_{sca}, σ_{bsca} and σ_{abs}) were conducted at several wavelengths using an integrating nephelometer (TSI model 3563) and an aethalometer (Magee Scientific model AE-31), since 2013 also with a Multi-Angle Absorption Photometer (MAAP, Thermo Scientific model 5012). The nephelometer measures scattering at blue, green and red wavelengths (450, 550 and 700 nm) and the aethalometer measures absorption at seven wavelengths ranging from the ultraviolet to the near-infrared (370, 470, 520, 590, 660, 880 and 950 nm). Here, absorption data from the AE-31 and scattering data from the TSI3563 were used since they have the longest time series, and an important part of our discussion is the analysis of trends. We used the MAAP data in determining a multiple scattering correction factor for the Aethalometer to get more accurate absorption measurements.

Both scattering and absorption measurements were recorded with a 5 minute resolution before June 2010 and after that with a 10 minute resolution. From June 2006 to June 2010, the measurements were conducted for the PM10 particles only and since

June 2010 also for the PM1 particles. The sample air is taken through a PM10 inlet (Digitel, Low volume inlet) and led alternatingly either directly to the instruments or via an impactor that removes particles larger than 1 µm in diameter.

2.2.2 Size distribution measurements

In addition to the AOPs~~optical measurements~~, ~~measurements of the~~ particle size distribution data were used in the analyses below. The size distributions ~~measurements~~ were ~~conducted~~measured with a Twin Differential Mobility Particle Sizer (TDMPS) in the size range 3–1000 nm (Aalto et al., 2001) and a TSI Aerodynamic Particle Sizer (APS, Model 3321) in the size range 0.53–10 µm. In the overlapping range of the TDMPS and the APS the number concentrations from the TDMPS were used up to 700 nm. The TDMPS, APS, integrating nephelometer and the aethalometer are located in the same measurement building. The TDMPS and APS have their own individual measurement lines. In the TDMPS measurement line, there is an inlet that removes particles larger than 1 µm. There is no active drying system in the TDMPS sample line to prevent particle losses. However, the sheath flows, which are used in the TDMPS system, are dried (RH < 40 %) so the particles are sampled in dry conditions. In the APS measurement line there is a pre-impactor that removes particles larger than 10 µm. The APS has its own dryer that heats up the sample air to 40 °C. This temperature might evaporate some semivolatile compounds, for instance ammonium nitrate but this is mainly an issue of urban sites (e.g. Bergin et al. 1997), whereas at the forest site in Hyytiälä low-volatile organic compounds are common (Ehn et al., 2014). Nevertheless, semivolatile aerosol particles are typically secondary particles smaller than 1 µm in diameter so evaporation of them does not have a large effect on the APS measurements.

2.3 Data processing

The data used in this study were measured between 21 June 2006 and 31 December 2017. All the optical data were quality assured manually and averaged for 1 h periods. The aerosol hygroscopic growth is often significant when RH increases above ~45 ± 5% and therefore the World Meteorological Organization and Global Atmosphere Watch (WMO and GAW) recommend for aerosol monitoring stations to keep sample air RH lower than that. In the GAW guidelines of 2003 the recommendation was to maintain RH < 50% but the limit was later lowered to RH < 40% (WMO/GAW, 2003, 2016). In the present work, if the internal RH in any of the optical instruments exceeded 40 %, the data from that instrument were excluded from further analysis if not stated otherwise. Note that Virkkula et al. (2011) followed the earlier RH recommendation: they calculated AOPs using data measured at RH < 50%. In addition, they also presented results from data measured at all RH. This affects comparisons of the results presented in this work.

All the optical data were also converted from ambient conditions to the standard temperature and pressure (STP) conditions (1013 hPa, 0 °C).

2.3.1 Scattering data

Both total~~The~~ scattering and backscattering coefficients measured with the nephelometer ~~w~~were~~as~~ corrected for the truncation error according to Anderson and Ogren (1998). The truncation correction uses the Ångström exponent (see Sect. 2.3.3) calculated from the uncorrected data.

Sherman et al. (2015) presented a well documented analysis for determining the uncertainty of the different AOPs. They determined a total fractional uncertainty of 9.2 % and 8.9 % (8.0 % and 8.1 %) for PM10 (PM1) σ_{sca} and σ_{bsca}.

To test, if excluding the moist data had a large effect on the AOPs and their trends, we included the periods of high humidity (RH > 40 %) in some of the analyses. However, in these cases we corrected the scattering data, which was flagged due to too high RH, to dry conditions by using the scattering enhancement factor *f*(RH). *f*(RH) describes the increase of σ_{sca} with increasing RH

$$f(\mathrm{RH}) = \frac{\sigma_{\mathrm{sca}}(\mathrm{RH})}{\sigma_{\mathrm{sca}}(\mathrm{RH{=}\ dry})}. \quad (1)$$

f(RH) is the ratio of σ_{sca} measured at high RH and at dry conditions. The *f*(RH) can be described by empirical relationship

$$f(\mathrm{RH}) = q\left(1 - \frac{\mathrm{RH}}{100\ \%}\right)^{-\gamma}, \quad (2)$$

with a parametrization presented by Zieger et al. (2015) for aerosol particles measured at SMEAR II in summer. They determined mean values for q and γ that were 0.96 ± 0.07 and 0.24 ± 0.07 at red wavelength (450 nm), 1.01 ± 0.05 and 0.25 ± 0.07 at green wavelength (525 nm), and 1.01 ± 0.05 and 0.30 ± 0.08 at red wavelength (635 nm). We used this parametrization, when the RH was higher than 40 %. Zieger et al. (2015) presented parameterization for total scattering only so we did not correct the σ_{bsca} to dry condition.

This parametrization was also used for calculating the radiative forcing efficiency (see Sect. 2.3.3) in ambient RH.

2.3.2 Absorption data

The ~~aethalometer~~ reported flow by the aethalometer was corrected by comparing the flow ~~reported by the aethalometer~~ with the weekly flow measurements conducted at the station. The correction was applied by using a moving average of these

measurements (see Sect. S2.1). An average spot size diameter of 8.3 ± 0.~~1~~2 mm was measured from the old aethalometer filters by using a loupe measuring scale magnifier (Esch~~t~~enbach) with 0.1 mm accuracy and it was used instead of the spot size reported by the aethalometer.

Here, we corrected the Aethalometer data by using the correction algorithm described by Collaud Coen et al. (2010)

$$\sigma_{\mathrm{abs},i} = \frac{\sigma_{\mathrm{ATN},i} - a_{s,i}\bar{\sigma}_{\mathrm{sca},s,i}}{C_{\mathrm{ref}}\, L_{s,i}}, \quad (3)$$

where

$$L_{s,i} = \left(\frac{1}{l\left(1-\bar{\omega}_{0,s,i}\right)+1} - 1\right) \cdot \frac{\mathrm{ATN}_i}{50\ \%} + 1, \quad (4)$$

and

$$a_{s,i} = \bar{\zeta}^{d-1}_{\mathrm{sca},s,i} \cdot c \cdot \lambda^{-\bar{\alpha}_{sca,s,i}\cdot(d-1)}. \quad (5)$$

In Eqs. 3 and 4, the subscript *i* indicates the number of the measurement and the subscript *s* indicates the average properties of the aerosol particles that are embedded in the filter spot. The over lined parameters are mean values from the start of the filter spot to the *i*th measurement. In Eq. 3, the σ_{ATN} is the attenuation coefficient reported by the Aethalometer, a is the scattering correction parameter, C_{ref} is the multiple scattering correction factor, and L is the loading correction function. In Eq. 4, the ω_0 is the single scattering albedo (see Sect. 2.3.3) and the ATN is the light attenuation through the filter spot in percentages. In Eq. 5 the ζ_{sca} is the proportionality constant of the wavelength power law dependence of σ_{sca} and α_{sca} is the Ångström exponent of the σ_{sca} (see Sect. 2.3.3). For l, d, and c we used values 0.74, 0.564 and $0.329 \cdot 10^{-3}$ respectively. For scattering correction, we used measured σ_{sca} values that were interpolated and extrapolated to the AE-31 wavelengths. Note that most of the symbols used for the variables are different from Collaud Coen et al. (2010). The reason is that in the present work the symbols are used for other variables below.

The C_{ref} was determined by comparing the Aethalometer data, that was corrected only for the filter loading artefact, against the reference absorption coefficient ($\sigma_{\mathrm{abs,ref}}$) measured by the MAAP.

$$C_{\mathrm{ref}} = \frac{\sigma_{\mathrm{ATN}}}{L \cdot \sigma_{\mathrm{abs,ref}}}. \quad (6)$$

The resulted median value for C_{ref} was 3.19, with a standard deviation of 0.67.

The uncertainty of the σ_{ATN} was determined according to Backman et al. (2017)

$$\frac{\delta\sigma_{\mathrm{ATN}}}{\sigma_{\mathrm{ATN}}} = \sqrt{f_{\mathrm{A}}^2 + f_{\mathrm{Q}}^2 + \left(\frac{\delta\sigma_{\mathrm{ATN,zero}}\Delta t_{\mathrm{zero}}}{\sigma_{\mathrm{ATN}}\Delta t_{\mathrm{avg}}}\right)^2}, \quad (7)$$

where the f_A and f_Q are the fractional uncertainties of the Aethalometer spot size and flow, which we determined to be 4.9 % and 1.5 % respectively; $\delta\sigma_{ATN,zero}$ is the standard deviation of the zero measurements; Δt_{zero} is the averaging time of the zero measurements; and Δt_{avg} is the averaging time of the measuremetns. For the uncertainty of σ_{abs} we took into account the fractional uncertainty of the C_{ref} that was f_C = 21 %

$$\frac{\delta\sigma_{abs}}{\sigma_{abs}} = \sqrt{\left(\frac{\delta\sigma_{ATN}}{\sigma_{ATN}}\right)^2 + f_C^2}. \quad (8)$$

At 520 nm, the uncertainty of σ_{abs} ranges from 22 % to 24 % if the σ_{ATN} varies from 14.2 Mm^{-1} to 1.3 Mm^{-1}, which are the 10th and 90th percentiles of σ_{ATN}. In this estimation of uncertainty, we did not take the uncertainty of scattering correction into account.

In calculating the single-scattering albedo and in iterating the complex refractive index, the absorption data had to be interpolated to the same wavelength with the scattering measurements. The absorption data were then interpolated to the blue, green, and red -wavelengths (450, 550, and 700 nm), using the Ångström exponent (α) described in Eqs. 11 and 12.

2.3.3 Intensive optical properties

The extensive ~~properties~~AOPs, which are the scattering, backscattering, and absorption coefficients (σ_{sca}, σ_{bsa}, and σ_{abs}), were used to calculate intensive properties presented in detail below.

The single-scattering albedo (ω_0) describes how much of the total light extinction (sum of σ_{sca} and σ_{abs}) caused by the aerosol particles is due to scattering:

$$\omega_0 = \frac{\sigma_{sca}}{\sigma_{sca} + \sigma_{abs}} \quad (9)$$

The ω_0 can be linked with the source and chemical composition of the aerosol particles. High values of ω_0 mean that the aerosol particles are mostly scattering and are light in color. Darker aerosol particles, which have a lower ω_0, have a relatively higher mass fraction of absorbing material, such as soot that is emitted in combustion processes.

The backscatter fraction (b) describes how much aerosol particles scatter radiation in the backward hemisphere compared with the total scattering

$$b = \frac{\sigma_{bsca}}{\sigma_{sca}}. \quad (10)$$

The angular dependency of particle scattering is dependent mostly on the particle size. The value of b is smaller for a size distribution that consists of larger particles, since large particles scatter light heavily in the forward direction and thus b can be used as an indicator of the shape of the particle size distribution. The b is an especially important property for modeling the

direct effect of aerosol particles on the climate, since it is used to describe how much sunlight is scattered upwards back into space.

The Ångström exponent (α) is used to describe the wavelength (λ) dependency of a certain optical property (σ) (Ångström, 1929)

$$\alpha = -\frac{\ln\frac{\sigma_1}{\sigma_2}}{\ln\frac{\lambda_1}{\lambda_2}}. \quad (11)$$

After calculating α, the optical property can be extrapolated or interpolated into different wavelengths

$$\sigma_1 = \sigma_2 \left(\frac{\lambda_1}{\lambda_2}\right)^{-\alpha}. \quad (12)$$

In this study, α values were calculated for σ_{sca} and σ_{abs} to obtain α_{sca} and α_{abs}.

Since light scattering is highly dependent on particle size, α_{sca} is also used as an indicator of the particle size distribution and is larger for the smaller particles, since they have a stronger wavelength dependency. If α_{sca} is larger than 2, ~~it is typically believed that~~ the volume distribution is typically dominated by particles smaller than 0.5 µm, and if α_{sca} is smaller than 1, ~~the~~ larger particles (physical diameter D_p > 0.5 µm) predominate in the distribution (Schuster et al., 2006). In comparison to b, α_{sca} is more sensitive to the coarse mode particles (e.g. Collaud Coen et al., 2007).

The value of ~~α_{abs} is also dependent~~depends also on the chemical composition, coating, and size of the particles, even though the chemical composition is generally considered to be the more important factor. The α_{abs} is usually used to identify black carbon (BC) and brown carbon (BrC) particles. The BC particles are highly absorbing aerosol particles and the BrC particles are considered to consist of some organic carbon compounds that absorb light more strongly at short than long wavelengths. If the particles consist purely of BC, the absorption would have a wavelength dependence of approximately λ^{-1} and α_{abs} would be equal to unity. However, if the particles also consist of material that absorbs light only at ultraviolet wavelengths, α_{abs} would be larger than 1. In ageing processes the BC particles may become coated by some purely scattering material, such as sulfuric acid or ammonium sulfate, or by slightly absorbing organic material (Schnaiter et al., 2005; Zhang et al., 2008). The coating greatly affects the absorption wavelength dependency, and thus the division into BC and BrC by considering only α_{abs} is not that simple. If the sizes of the BC particles and the thickness and complex refractive index (m) of the coating are not known, it is challenging to use α_{abs} to describe the chemical composition of the particles (Gyawali et al., 2009; Lack and Cappa, 2010). In spite the fact that the α_{abs} depends also on the coating, ~~T~~the absorption wavelength dependency is often used to describe the source of the BC (Sandradewi et al., 2008; Zotter et al., 2017). The source apportionment assumes that there are BC emissions only from traffic and wood burning and that the BC from these sources has a specific wavelength dependency.

To investigate how the AOPs at SMEAR II would affect the climate, the aerosol radiative forcing efficiency ($\Delta F\delta^{-1}$ or RFE) was also calculated. The RFE is a simplified formula that describes how large a difference the aerosol particles would make to the radiative forcing (ΔF) per unit of aerosol optical depth (δ) (Sheridan and Ogren, 1999)

$$\frac{\Delta F}{\delta} = -DS_0T_{at}^2\omega_0\beta(1-A_c)\left[(1-R_s)^2 - \left(\frac{2R_s}{\beta}\right)\left(\frac{1}{\omega_0}-1\right)\right]. \quad (13)$$

RFE does not take into account that the properties and amount of aerosol particles vary vertically in the atmospheric column. In the Eq. ~~11~~13, D is the fractional day length, S_0 the solar constant, T_{at} the atmospheric transmission, A_C the fractional cloud amount, and R_S the surface reflectance for which the following constants were used respectively: D = 0.5, S_0 = 1370 Wm^{-2}, T_{at} = 0.76, A_C = 0.6 and R_S = 0.15. The values were according to Haywood and Shine (1995), who used these values independent of wavelength in calculating the ΔF. Sheridan and Ogren (1999) used these same constants later in calculating the RFE at 550 nm. In this study we determine the RFE at 550 nm. The factor β is the upscatter fraction and is calculated using b (Delene and Ogren, 2002)

$$\beta = 0.0817 + 1.8495b - 2.9682b^2. \quad (14)$$

It must be noted that Eq. 14 does not take into account the variation in the sun's zenith angle.

As stated by Sherman et al. (2015), the purpose of determining the RFE is to provide a means for comparing the intrinsic aerosol forcing efficiency of aerosols measured at different sites. We calculated the RFE by using the constant values to have results comparable with other studies in very different types of environments (e.g. Sheridan and Ogren, 1999; Andrews et al., 2011; Sherman et al., 2015; Shen et al., 2018) and to study how the RFE changes with varying ω_0 and b. Here we refer the RFE that was calculated by using the above-mentioned constant values as $RFE_{H\&S}$. It must be noted that ω_0 and b used in Eq. 13 are defined for dried sample air; thus $RFE_{H\&S}$ does not represent ambient air. In the ambient air, RH is larger and the AOPs change due to hygroscopic growth.

In addition to $RFE_{H\&S}$, we calculated a seasonal RFE by allowing the D to vary and by using more realistic seasonal values for A_C, and R_S. The seasonal variations of these parameters are presented in Fig. S1. Here we refer the seasonal RFE as RFE_S. The effect of ambient RH on ω_0 and b, and hence to RFE, was also studied. The seasonal RFE calculated for ambient RH is referred as $RFE_{S,moist}$. More information about the seasonal D, A_C, R_S, and RH can be found in the supplementary material Sect. S2.

Seasonal A_C was derived by using a ceilometer data. The ceilometer was deployed at the Halli airport (about 25 km from SMEAR II) by Finnish Meteorological Institute (FMI) in 2010. The data were averaged for each month to get a seasonal variation. The lowest mean A_C was in July (~0.25) and the highest in January (~0.76).

For the seasonal R_S, reflectivity determined by Kuusinen et al. (2012) was used. They determined the R_S in a boreal forest for different amounts of canopy snow cover. According to the FMI, the average season of snow cover in Hyytiälä is from 16

November to 20 April (FMI: http://ilmatieteenlaitos.fi/lumitilastot, in Finnish only, last accessed: 13 March 2019) and for that time period we used $R_S = 0.314 \pm 0.14$ that Kuusinen et al. (2012) determined as the average albedo for a snow covered canopy. For snow-free forest we used $R_S = 0.126$, which is an average of the mean monthly albedos Kuusinen et al. (2012) determined for snow-free months.

In calculating the ω_0 for ambient air, we used the equations (Eqs. 1 and 2) and parametrization presented in Sect. 2.3.1 to convert the σ_{sca} for ambient RH; σ_{abs} was assumed to be constant with increasing RH, as Nessler et al. (2005) showed that the change in the σ_{abs} with increasing RH is very small compared to scattering. There has not been measurements of hygroscopic growth parameters (q and γ) for σ_{bsca}, so we could not use the same parametrization in calculating the b to ambient RH. Fierz-Schmidhauser et al. (2010) observed about 30 % decrease in b when the RH increased to 85 % at the Jungfraujoch measurement station. We used this observation as a linear approximation to estimate the how the b changes with varying RH. The estimated b was then used in calculating the β for moist conditions. The seasonally averaged RH was determined from RH measurements conducted at the height of 16 m. The lowest mean RH occurred in May (~62 %) and the highest in November (~95 %).

The estimated uncertainties for the intensive AOPs are presented in Sect. S3 in the supplementary material. The uncertainties were calculated according to Sherman et al. (2015).

2.3.4 Data coverage

If averaged over the whole measurement period, 81 % of the nephelometer data and 70 % of the aethalometer data were considered valid. All the AOPs had some gaps in the data (see Fig. 1). Monthly data coverage of σ_{sca} and σ_{abs} are presented in Table S1. Most of the gaps in the time series of AOPs during the summers of 2006 to 2010 were due to too high RH. The gap in 2010 was due to maintenance and installation of the dryers and the switching inlet system. Some additional σ_{bsca} data were missing, due to malfunction of the backscatter shutter of the integrating nephelometer. Dirty optics, malfunctions and maintenance caused the gaps in the σ_{abs} data in 2012 and 2015.

Until March 2010, the integrating nephelometer and the aethalometer measured sample air that was not dried with any external dryers. During winter, the relative humidity (RH) remained below 40 %, since the sample air warmed up to room temperature (about 22 °C). Sometimes in summer, the RH of the sample increased to over the 40 % limit. If the RH was above 40 %, the data were flagged as invalid and they were omitted from the data analysis if not stated otherwise. About 25 % of all the data before March 2010 had to be removed due to too high RH. Almost all of the removed data was from summer and fall months (June – October) and if regarding only these months, 46 % of the data were flagged. If the moist data was included the overall data coverage would increase to 89 % and 77 % for scattering and absorption data, respectively. After the installation of the Nafion-dryers in March 2010, the humidity caused no further problems.

2.4 Properties calculated from particle size distributions

With the size distributions it is possible to calculate differently weighted mean diameters. In this study, we used the geometric mean diameter (GMD) and the volume mean diameter (VMD). The GMD is the mean diameter that is weighted by the number concentration (N)

$$\mathrm{GMD} = \exp\left(\frac{\sum N_i \ln D_{p,i}}{\sum N_i}\right), \quad (15)$$

while the VMD is weighted by the particle volume (V)

$$\mathrm{VMD} = \frac{\sum D_{p,i} V_i}{V_{tot}} = \frac{\sum N_i D_{\mathrm{p},i}^4}{\sum N_i D_{\mathrm{p},i}^3}. \quad (16)$$

Since the number concentration is focused on the nucleation and Aitken mode particles, the GMD describes the distribution changes in the smallest sizes. The VMD, in contrast, is affected by the changes in the accumulation and coarse mode, since they contribute the most to the volume size distribution.

The measurements of the AOPs and size distribution can be combined by determining the complex refractive index ($m = n + ik$) that describes how much the particles scatter and absorb light and can be used to model σ_{sca}, σ_{bsca} and σ_{abs} from the size distribution measurements. Index m consists of the real part (n), which accounts for the scattering, while the absorption is described by the imaginary part (k). Like ω_0, m provides information on the darkness and the chemical composition of the aerosol particles.

In this study, m was iterated from the σ_{sca}, σ_{abs} and size distribution measurements in a manner similar to that described by Virkkula et al. (2011). In the first step of the interpolation $\sigma_{sca,Mie}$ and $\sigma_{abs,Mie}$ were determined for the measured size distribution by using the Mie-theory with initial $m = 1.544 + 0.019i$. The calculated $\sigma_{sca,Mie}$ and $\sigma_{abs,Mie}$ were then compared with the measured σ_{sca} and σ_{abs}. If the calculated and measured values did not agree the real part of m was first varied stepwise by 0.001 until the measured and modeled σ_{sca} agreed. Next, the imaginary part of m was varied in the same way until the measured and modeled σ_{abs} agreed. This iteration was continued until the measured and calculated values agreed within 1 %. The new imaginary part of m also affected σ_{sca} so the real part had to be reiterated. ~~This iteration was continued until the measured and calculated values agreed within 1 %.~~ The MATLAB codes developed by (Mätzler, 2002) were used to model the Mie scattering and absorption.

2.5 Trends

The trends and their significance were determined using the seasonal Kendall test described by Gilbert (1987). This test determines if there is a similar trend for each season (month) separately. All of the trends were calculated for the monthly medians, and at least 14 days of valid data in a given month were required for this month to be taken into account in the trend analysis.

3 Results and discussion

Below we first present the descriptive statistics of the AOPs, their trends, and seasonal variations at SMEAR II. The figures of the AOPs in this section are presented in the green wavelength (550 nm for the scattering and intensive properties and 520 nm for the absorption measurements). In the figures of α_{sca} and α_{abs}, wavelength ranges of 450–700 nm and 370–950 nm were used. The results are presented for dry aerosols (RH < 40 %) if not stated otherwise.

3.1 Overview of the data

The descriptive statistics of the AOPs of both the PM10 and PM1 particles are shown in Tables 1 and 2, respectively. From Table 1~~Table 1~~ we see that the PM10 AOPs differ somewhat from the results of Virkkula et al. (2011) and Pandolfi et al. (2018) that can be explained by the trends and by differences in the data processing. For example the mean σ_{sca} (~15 Mm^{-1}) at λ = 550 nm in this study was lower than that presented by Virkkula et al. (2011) (~18 Mm^{-1}) and by Pandolfi et al. (2018) (~17 Mm^{-1}), which is probably due to the tendency of σ_{sca} to decrease (see Sect. 4.2). Another reason is that in the data processing Virkkula et al. (2011) used the earlier WMO/GAW recommendation (WMO/GAW, 2003) and used data measured at RH < 50% and did not do any RH corrections. We also determined a strong tendency for σ_{abs} to decrease as well, but the mean σ_{abs} (~2.1 Mm^{-1}, interpolated to 550 nm) was not much lower than the mean (~2.2 Mm^{-1}, at 550 nm) in the study by Virkkula et al. (2011). This was due to the differences in the aethalometer data-processing. Virkkula et al. (2011) reported no flow or spot size corrections and they used the algorithm of Arnott et al. (2005) and C_{ref} = 3.688 at λ = 520 nm. Naturally, the different methods used in the absorption data processing also affected the optical properties that are dependent on the σ_{abs}, such as ω_0 and k. In the correction algorithm by Arnott et al. (2005), the C_{ref} is wavelength depended, which increases the α_{abs}. Virkkula et al. (2011) reported a median α_{abs} = 1.4 that is notably higher than the median α_{abs} = 1.0 determined by our study. The difference in α_{abs} can be attributed to the correction algorithm since also in the present work the average and median α_{abs} = 1.36 and α_{abs} = 1.34 for the wavelength range 370–950 when the Arnott et al. (2005) algorithm is used. (see Table S2).

In comparison to similar studies conducted at other Finnish measurement stations at Pallas in northern Finland (Lihavainen et al., 2015) and at Puijo tower in Kuopio, eastern Finland (Leskinen et al., 2012), SMEAR II showed the highest σ_{sca} and σ_{abs} measured for PM10 particles. At SMEAR II, σ_{sca} was about two times higher and σ_{abs} about three times higher than at Pallas, where the mean values of σ_{sca} = 7.9 Mm^{-1} and σ_{abs} = 0.7 Mm^{-1} were measured at green wavelength. The Pallas station is remote, located 170 km north of the Arctic Circle, far from anthropogenic sources. At SMEAR II, σ_{sca} and σ_{abs} were about 1.~~4~~3 and 1.1 times higher~~, respectively~~, than that measured at the Puijo tower, where the mean values of σ_{sca} = 11.6 Mm^{-1} and σ_{abs} = 1.6 Mm^{-1} were measured at green and red wavelengths, respectively.~~, even though the~~ Puijo tower is a semi-urban measurement station located only 2 km away from the Kuopio city center. At the Puijo tower the measurements were conducted only on particles smaller than 2.5 µm, which explains part of the differences, at least for σ_{sca}.

Even though the σ_{sca} measured at SMEAR II is high compared to other measurements conducted in Finland, the air measured at SMEAR II is still clean when compared to other European stations. Due to the remote location, Pandolfi et al. (2018) observed rather low σ_{sca} at SMEAR II compared to other European sites. Lower median σ_{sca} was observed only in the arctic region, at another Nordic rural station in Birkenes, Norway, and at several high mountain sites~~The mean ω_0 was 0.84 for Puijo tower (at 637 nm), 0.88 for SMEAR II (at 550 nm), and 0.92 for the remote Pallas station (at 550 nm).~~. Highest σ_{sca} Pandolfi et al. (2018) observed in central and Eastern Europe.

The differences between the optical properties of the PM1 and PM10 particles are explained by the differences in concentrations, size distributions and chemical compositions. If only the PM10 data overlapping with the PM1 measurements were taken into account, the median values of σ_{sca}, σ_{abs}, ω_0, b, α_{sca}, α_{abs}, n, and k would have been 9.~~5~~6 Mm^{-1}, 1.3 Mm^{-1}, 0.89, 0.~~15~~14, 1.92, 0.~~96~~97, 1.525 and 0.014 (σ_{sca}, ω_0, b, α_{sca}, n and k at 550 nm, σ_{abs} at 520 nm), respectively. The extensive variables (σ_{sca}, σ_{bsca} and σ_{abs}) were smaller for the PM1 measurements, since there was less particle volume interacting with the radiation. Due to the differences in the median ω_0 and n, the PM1 particles absorbed more light relative to scattering than the PM10 particles. The α_{sca} and b are related to the sizes of the particles, so they were naturally different between the PM1 and PM10 particles. For the smaller PM1 particles, the α_{sca} and b were larger than for the PM10 particles. However, b does not have as large a difference between the PM1 and PM10 particles as α_{sca}.

The average values of the PM10 particles given in Table 1 are calculated by excluding the periods when the RH > 40 %. If these periods of σ_{sca} and σ_{abs} measurements were included in the analysis and the moist scattering data were corrected to dry conditions by using the Eqs. 1 and 2, we would get median values of σ_{sca} = 10.3 Mm^{-1}, σ_{abs} = 1.5 Mm^{-1}, ω_0 = 0.88, b = 0.15, α_{sca} = 1.91, α_{abs} = 0.98, and RFE$_{H\&S}$ = -23 for PM10 (σ_{sca}, ω_0, b, and RFE$_{H\&S}$ at 550 nm, σ_{abs} at 520 nm, α_{abs} at 370 nm/950 nm and α_{sca} at 450 nm/700 nm). The differences are not large compared to values presented in Table 1, so omitting the moist data periods from the data set does not seem to have a large effect on the median AOPs in this data set.

3.2 Trends

The long time series of the PM10 and PM1 AOPs were used to determine the trends for the optical properties. For the PM10 trend analysis we used data from about 10.5 years and for the PM1 trend analysis we used about 7.5 years long time series. The slopes of the trends and the trend statistics are presented in Table 3. The table also presents the trends as percentages, which were calculated by dividing the slope by the overall median value of the variable. The trends are also plotted in Fig. 1, where the monthly medians of the PM10 AOPs at SMEAR II used in this analysis are presented. The monthly medians are included in Fig. 1~~Fig. 1~~ only if the month had at least 14 days of valid data.

In the extensive properties, the trends were negative. The slopes of the trends for PM10 σ_{sca}, σ_{bsca} and σ_{abs} were -0.32, -0.038, and -0.~~088~~ 086 $Mm^{-1}yr^{-1}$, respectively. The decrease in the extensive properties were due to decrease in the total particle number concentration (N_{tot}) and total volume of the particles (V_{tot}) that can be seen in the combined TDMPS and APS data presented in Figs. 2a and b~~Figs. 2a and b~~ and in Table 3. The relative decrease in V_{tot} (-4 $\%yr^{-1}$) was rather similar to that of σ_{sca} (-3 $\%yr^{-1}$). Also, Pandolfi et al. (2018) showed a statistically significant trend for σ_{sca} (-0.588 $Mm^{-1}yr^{-1}$) measured at SMEAR II. They reported negative trends at other European sites as well and they determined that the average decrease was about -35 % for a ten-year period, which is a bit larger reduction than that observed at SMEAR II (-30 % for a ten-year period). The results are in line with the decrease in particle number concentration observed in European countries (Asmi et al., 2013). Also the remotely measured decreasing trend for aerosol optical depth (δ) supports the decreasing trends in Europe (Li et al., 2014). Decreasing trends for σ_{sca} are not only observed in Europe; Collaud Coen et al. (2013) and Sherman et al. (2015) reported negative trends for σ_{sca} in North America as well.

The observed relative decrease in σ_{abs} (-6 $\%yr^{-1}$) was about twice as large than that of σ_{sca} (-3 $\%yr^{-1}$). The differences in the trends indicates that during the measurement period, the amount of absorbing material, such as BC and BrC, decreased relatively faster than the amount of scattering material (e.g. sulfate). It is also possible that the decrease in non-absorbing compounds decreased the σ_{abs} since a non-absorbing coating around an absorbing particle can act as a lens, which increases absorption. The study by Collaud Coen et al. (2013), which included also σ_{abs} data, observed negative trends for both σ_{sca} and σ_{abs} at the Bondville measurement station in Illinois, USA. There the trends of σ_{sca} and σ_{abs} were similar in magnitude (about -3 % yr^{-1}). Sherman et al. (2015) did not observe this decreasing σ_{abs} trend later.

For the PM1 σ_{abs}, we observed a very steep decrease (-12 % yr^{-1}), which was probably caused by very high σ_{abs} measured in January and February in 2012. Also, the data gaps in winter 2013 and 2015 could have affected the trends. The time series, of which the trends were determined for the PM1 measurements, were only 7.5 years long. Trends, which are determined for shorter time series, are more sensitive to year-to-year variability. This kind of extreme values can induce relatively large trends, which is why trend analysis for short time series (less than ten years) should be treated with caution.

Since the aerosol particles were absorbing less light than before, there was a tendency for the ω_0 to increase. As shown by the increase in ω_0 and the decrease in the extensive properties, the air measured at SMEAR II was less polluted than before. The higher ω_0 indicates that the measurements were less affected by particles produced by traffic emissions or incomplete combustion. Li et al. (2014) reported mostly positive trends that were determined by remote measurements conducted in Europe. The decreasing trend for k supports the tendency for ω_0 to increase, since the negative trend for the imaginary part of m means that particles absorb less light. The α_{abs}, which is also related to the chemical composition of the particles, showed no significant trend for either the PM1 or PM10 particles. The negative trend for the interpolated n was only significant for the PM1 particles. The tendency for the interpolated n to decrease could have been caused by changes in the chemical composition.

The trends of the b and α_{sca} were also investigated. These trends describe how the size distribution of the aerosol particles has changed. For the PM10 b and α_{sca} the trends were positive, but for the PM10 α_{sca} however, the p value was 0.07 so there was only a weak evidence for the positive trend in PM10 α_{sca}. For the PM1 the trends for both, b and α_{sca}, were positive and statistically significant. Increasing b and α_{sca} indicates that the mean size of the size distribution was moving towards smaller particles. The shift of in the size distribution towards smaller diameters is also observed in the negative trend of the volume mean diameter (VMD_{tot}), presented in Fig. 2c and in Table 3, supporting the increase in b and α_{sca}.

Also, Pandolfi et al. (2018) observed increasing trends for b at SMEAR II and other European stations. For the α_{sca}, however, they observed both positive and negative trends at different stations. Pandolfi et al. (2018) suspected that the variation was caused by differing trends of the coarse and accumulation mode particle concentration. Li et al. (2014) observed negative trends for the α_{sca} across the Europe and they suggested the trends were caused by a decrease in fine particle emissions.

Since the trends of b and α_{sca} for the PM10 and PM1 measurements were similar, the trends in α_{sca} and b may indicate that the concentration of larger particles in the accumulation mode was decreasing, since a decrease in coarse particle concentration only could not cause the decreasing trend of PM1 α_{sca}. The changes in the size distribution were investigated by determining a trend for each TDMPS and APS measurement channels. The results, which are presented in Fig. S4, pointed out that relatively greatest decrease occurred for accumulation mode particles that were 500 – 800 nm in diameter. On average, the volume size distribution of accumulation mode particles peaks around 300 nm (see Figs. S6 and S7) so the greatest decrease occurred at the larger sizes of the accumulation mode. The decrease in this size range might be caused by decrease in long-range transported pollution. Aged pollution particles might be grown by other substances, such as SO_2 in the atmosphere so their sizes are larger than freshly emitted or formed particles. SO_2 emissions have decreased in Europe (Tørseth et al., 2012), which supports this assumption. A trajectory analysis by Virkkula et al. (2011) showed that α_{sca} was clearly higher in air masses from continental Europe than from the North Atlantic and but also that the highest α_{sca} values were measured in air masses sources from within southern Finland, which would suggest that larger particles are not from nearby the station.

The installation of the Nafion-dryers in 2010 could have caused an artificial decrease in σ_{sca} or σ_{abs} since the dryers increase the deposition of the particles and may decrease the sizes of hygroscopic particles. However, the trends were similar for the PM10 and PM1 particles. During the PM1 measurements, there were no large changes in the measurement line, so the observed trends were probably not caused by any technical changes in the measurement line.

A lot of summer time data measured before 2010, were marked invalid due to too high humidity and it could have affected the trend analysis. To test this hypothesis, we used Eqs. 1 and 2 to correct the σ_{sca} to dry conditions and included this data in the trend analysis. The σ_{bsca} was not corrected to dry conditions. Also, moist (RH > 40 %) absorption data was included in this test. Including the originally omitted data in the trend analysis, we observed statistically significant (p-value < 0.05) trends for the PM10 σ_{sca}, σ_{abs}, ω_0, and RFE with the slopes of -4 % yr^{-1}, -5 % yr^{-1}, 0.2 % yr^{-1}, and 0.5 % yr^{-1} respectively. Still, there were decreasing trends for extensive properties and positive trends for ω_0. However the difference between the σ_{sca} and σ_{abs} trends decreased from 3 % to 1 % if compared against the trends that were determined only for the dry conditions. Including the moist data and acquiring longer data sets in the trend analysis suggests that the relative difference between the trends of σ_{sca} and σ_{abs} might not be that large. Not correcting the σ_{bsca} to dry conditions probably explains why we do not see a significant trend for the b here.

In addition to the general trends, we also investigated how the trends of σ_{sca} and σ_{abs} varied between different seasons. In this analysis, the periods of RH > 40 % were included (σ_{sca} corrected to dry conditions according to Eqs. 1 and 2) in order to avoid the data gaps in summer and autumn before 2010. The trends were determined separately for spring (March, April, May), summer (June, July, August), autumn (September, October, November), and winter (December, January, February). The trend calculations were conducted by using the monthly medians (see timeseries in Fig. S3). The results are presented in Table 4.

Table 4 shows that σ_{sca} and σ_{abs} had a decreasing trend for each season, but for the autumn the trends were not significant. Both σ_{sca} and σ_{abs} experience the fastest absolute decrease in winter when the energy consumption is the highest and pollution sources are more pronounced; on the opposite, the trends are the least negative in summer. In spring, the absolute trends were less negative than compared to winter. However, for the σ_{abs} we observed that the relative trend in spring (-9 %yr^{-1}) was steeper than in winter (-8 %yr^{-1}).

3.3 Aerosol optical properties and size distribution

To obtain a better view on how the shape of the size distribution affected the AOPs, the various AOPs were compared against the GMD and VMD. The results of the comparison are shown in Fig. 3. The GMD was mostly affected by the small nucleation

and Aitken mode particles, which are high in number concentration; the accumulation mode particles also had some effect on the GMD. Since only the smallest particles affect the GMD it is practically the same for the fine (D_p < 1 µm) and total (D_p < 10 µm) particle size distribution. Thus we present the comparison of GMD and AOPs only for the PM10 particles (Figs. 3a – d). The VMD, however, was heavily affected by the size distribution of the accumulation and coarse mode particles, since they predominated in the particle volume size distribution. This explains why there was notable differences for the PM10 (Figs. 3e – h) and PM1 (Figs. 3i – l) particles, when their AOPs were compared against the VMD calculated for particles smaller than 10 µm (VMD_{tot}) and VMD calculated for particles smaller than 1 µm (VMD_{fine}), respectively.

The σ_{sca} correlated positively with the GMD due to the changes in particle concentration in the accumulation mode. The median number and volume size distribution for situations when GMD was below 50 nm or above 100 nm are presented in Fig. 4c. There was a clear difference in the number and volume size distribution in the accumulation mode when the GMD limit was varied. From the number size distribution, it can be seen that GMD increased due to a larger accumulation mode and lack of particles in the nucleation and Aitken modes. Nucleation and Aitken mode particles are mainly produced and grown by condensing vapors and since larger particles in the accumulation mode act as a condensation sink for vapors, the smaller particle modes do not tend to exist when accumulation mode particles are present.

For the PM10 particles, there was a negative correlation between the σ_{sca} and VMD, but when the coarse particles were ignored, i.e. for PM1 particles the correlation became positive. The negative correlation for the PM10 particles is caused by the changes in the accumulation and coarse mode particle concentration. This is shown in further detail in Fig. 4a, where the median volume size distribution is presented for situations in which the VMD_{tot} > 1500 nm, 500 nm < VMD_{tot} < 1000 nm and VMD_{tot} < 500 nm. When the VMD_{tot} was high, there was a strong coarse mode but the accumulation mode was clearly smaller than in the other situations. Even though the VMD_{tot} was high, the lack of accumulation mode particles decreased the scattering. From Fig. 3a~~Fig. 4a~~, it can be seen that the σ_{sca} became maximal when the VMD_{tot} was about 500–1000 nm. In this VMD range, the coarse mode was slightly smaller but the accumulation mode clearly increased, thus increasing the scattering. When the VMD_{tot} < 500 nm, the coarse mode was almost completely missing that caused the σ_{sca} to decrease, even though there was a large accumulation mode present.

Kulmala et al. (2016) estimated that fresh eBC particles observed at SMEAR II are in the size range of 80 – 120 nm. That estimate was calculated in a simplified way from the relationship between particle number concentrations and BCe concentrations. A better estimate is obtained from the size dependence of ω_o. The darkest aerosol has ω_o < 0.6 and GMD in the range of about 30 – 70 nm (Fig. 3b, 3f, and 3j). This has been shown to be the range of fresh BC (e.g., Kittelson, 1998; Casati et al., 2007; Zhang et al., 2008) which suggests the source of BC is not far, probably within some kilometers only.

The size-dependent properties α_{sca} and b for PM10 acted rather differently when compared with the GMD and VMD_{tot}. The~~When the GMD was higher, the~~ α_{sca} ~~also~~ increased with growing GMD (Fig. 3c), which ~~that~~ is in contrast with the expectation that the α_{sca} would decrease when the size distribution is dominated by larger particles. The observation that the α_{sca} increased with an increasing GMD is in line with the analyses made for AOPs and size distributions measured in Guangzhou, China by Garland et al. (2008), at SMEAR II by Virkkula et al. (2011), and in Nanjing, China by Shen et al. (2018). To study the reasons behind this relationship we generated first unimodal size distributions with two geometric standard deviations GSD = 1.5 and 2.0 and calculated both σ_{sca} and σ_{bsca} at λ = 450, 550, and 700 nm with the Mie code with m = 1.517 + 0.19i and the α_{sca} and b from them. For unimodal size distributions the α_{sca} decrease~~d~~ with increasing GMD~~,~~ as is shown by the lines in Fig. 3c. ~~They were calculated by generating unimodal size distributions with the geometric standard deviations GSDs = 1.5 and 2.0 and calculating the σ_{sca} for λ = 450, 550, and 700 nm with the Mie code with m = 1.517 + 0.19i and the α_{sca} from them.~~ Schuster et al. (2006) showed that the relationship may be the opposite for ~~a~~ bimodal size distribution~~s~~. Schuster et al. (2006) explained this behavior by that adding a larger or coarse particle size mode to a fine particle mode that is inefficiently scattering - for instance nucleation and Aitken mode particles – the larger mode contributes more efficiently to the Ångström exponent than the fine mode. The contribution of the particles smaller than 100 nm to GMD is larger than that of the larger particle modes which leads to the observed relationship. To study this in more detail we generated also bimodal size distributions. The analysis presented in the supplement (S6) shows that the α_{sca} of bimodal size distributions can be calculated as a linear combination of the α_{sca} of the modes, weighted by the fractions of σ_{sca} of the respective modes. This explains the increase of α_{sca} with growing GMD.

In addition, ~~A~~at SMEAR II the size distribution typically consists of not only two but ~~of~~ multiple modes (Dal Maso et al., 2005; Saarikoski et al., 2005) that explains the observed relationship. An additional qualitative analysis of this relationship is given in Fig. 4c, where the median number and volume size distributions are plotted for situations in which the GMD was < 50 nm and > 100 nm. By comparing these two situations, it can be seen that when the GMD > 100 nm the accumulation mode was much larger than when GMD < 50 nm. Since the coarse mode is rather similar for both cases, the α_{sca} varied due to changes in the accumulation mode. For the α_{sca} and VMD, the correlation was negative (Fig. 3g) that supports the expectations. However, the α_{sca} measured for the PM10 particles was much higher than that modeled for the unimodal distributions, which can also be explained by the multiple modes of the real size distributions.

There was a negative correlation between the GMD and PM10 b (Fig. 3d) as expected, but the correlation was rather weak. On the contrary, the correlation between the VMD_{tot} and PM10 ~~α_{sca}~~ b was slightly positive (Fig. 3h). The ~~positive~~ negative correlation of α_{sca} with VMD_{tot} and the ~~negative~~ positive correlation of b with VMD_{tot} for the PM10 particles indicates that the

α_{sca} and b were sensitive to different size ranges. The α_{sca} decreased when there are more coarse particles present, but for the b the coarse particles seem to have no expected effect and the b increased with increasing VMD_{tot}. Fig. 4a. shows that when the VMD > 1500 nm, the peak of $DV/d\log D_p$ in the accumulation mode was much lower and tilted towards the smaller diameters than compared to the situations where the VMD < 1000 nm. This is in line with Collaud Coen et al. (2007), who stated that in the Jungfraujoch data, b was sensitive to particles smaller than 400 nm and that the sensitivity of the α_{sca} was at its maxima for particle diameters between 500 and 800 nm.

For the PM1 particles, the measured α_{sca} and b were well in line with the modeled values (Figs. 3k and l), since the coarse mode particles were removed prior to the measurements, the shape of the size distribution was closer to a unimodal size distribution, and the VMD_{fine} described better how the accumulation mode shifted.

3.4 Seasonal variation

The seasonal variation in the PM10 AOPs was clearly visible in the 12-year record shown in Fig. 5. The seasonal variation in σ_{sca} and σ_{bsca} (Figs. 5a and b) was not yet as clear in Virkkula et al. (2011) as it is now. For the σ_{sca} and σ_{bsca}, two local maxima occurred during late winter (February) and late summer (July). The local minima occur during spring (April) and late autumn (October). The σ_{abs} showed the highest values during winter (February) and the lowest values during summer (June). Part of this variation is explained by boundary layer dynamics. In summer, the boundary layer is higher and well mixed thus diluting the aerosol concentration. In winter the situation is the opposite and the pollution accumulates in the shallow boundary layer.

For the extensive properties, the highest values occurred at the same time in winter (February) when the ω_0 was also low, which means that there were larger amounts of particles from anthropogenic sources than in summer. Hyvärinen et al. (2011) observed increased equivalent eBC concentrations at SMEAR II in winter, when the long-range transport brings pollution from the central and eastern Europe. However, Hienola et al. (2013) estimated that about 70 % of the measured eBC at SMEAR II is emitted from local or regional sources or transported from Finnish cities so also the local and regional emissions have a significant role in the elevated eBC concentrations. Since February is one of the coldest months in Finland, domestic wood burning in the local and regional area increases the particle concentration (Karvosenoja et al., 2011). Pollution can also be transported from nearby cities (the largest and closest are Tampere and Jyväskylä). Hyvärinen et al. (2011) observed no remarkable changes in the Hyytiälä eBC concentrations coming from the Tampere region. However, the largest concentrations they observed came from the direction of Orivesi, a small town (population about 9 000) 20 km from the measurement station.

In summer, the ω_0 had its highest values since the σ_{sca} was high and the σ_{abs} was low. In summer, the anthropogenic influence is not as strong as in the winter since the energy consumption is lower. The contribution of particles from natural sources

increased during spring and summer when the vegetation was active and growing. The seasonal variation in the n and k was clearly associated with the ω_0. In summer when the ω_0 was high, n was high and k was low. In winter, the relationship was the opposite. The scattering maximum in summer was probably caused by secondary organic particles (Tunved et al., 2006) explaining why the b and α_{sca} are also maximal.

There is an anti-correlation between the seasonal variations of ω_0 and α_{abs}. The maximum values of α_{abs} (> 1) occur in winter, which means that light is absorbed more efficiently at shorter wavelengths than in summer. A higher α_{abs} may suggest that light is absorbed not only by BC, but also by some light-absorbing organic carbon compounds, i.e. brown carbon (BrC). In using only α_{abs}, it is difficult to determine if the particles consist of BrC, since BC particles with coating can also have an α_{abs} up to 1.6 (Lack and Cappa, 2010). In Fig. 5 we can see that the value of 1.6 is not really reached at SMEAR II. Since α_{abs} is dependent on the size of the BC core, the thickness of the coating and the m of the coating, more detailed investigation would be needed to determine why α_{abs} is varies.

Also, the α_{abs} is typically associated with the source of the BC and it is often used to quantify whether the BC is traffic or wood burning related (Sandradewi et al., 2008; Zotter et al., 2017) so that high α_{abs} is a sign of wood burning. In the source apportionment, α_{abs} close to one indicates that the BC is sourced from traffic. Since we observed relatively higher α_{abs} in winter, the results are in line with the assumption of domestic wood burning that takes place during winter. However, in summer, α_{abs} was often < 1, which would yield an unphysical fraction (over a 100 %) of traffic related BC. Values below 1 could have been caused by large BC particles (D_p > 100 nm) that have a purely scattering coating (Lack and Cappa, 2010). It must be noted that the α_{abs} depends also on the correction algorithm. For example, if the σ_{abs} was corrected with the algorithm proposed by Arnott et al. (2005), the mean ± SD of α_{abs} would have been 1.36 ± 0.51 (see Table S2). Using the α_{abs}, which was determined by using the correction by Arnott et al. (2005), the results for the source apportionment would be different and they would show higher fraction of BC from wood burning. Further investigation of the complex nature of α_{abs} is omitted here.

The seasonal variation in α_{sca} and b depends on the seasonal variation in the size distribution of the particles. Both α_{sca} and b were maximal in summer and minimal in winter, suggesting that in summer, the particle population consisted of smaller particles than in winter. Closer investigation on the size distribution, which is presented in Fig. S6 and S7, reveals that in winter, the VMD_{tot} was experiencing it minimum due to a lack of coarse mode particles. This is in contrast with the observation or smaller α_{sca} and b. In fact, the seasonal variation of α_{sca} and b was explained by the seasonal variation of accumulation mode and VMD_{fine}, which is a good indicator for the shifting accumulation mode. In winter, the accumulation mode was shifted towards larger sizes and the median of VMD_{fine} was about 350 nm. In summer the situation was the opposite and VMD_{fine} was about 250 nm.

3.5 Variation between the PM10 and PM1 measurements

Even though the average values between the optical properties of the PM10 and PM1 particles differed, their seasonal variation was similar for all the various properties. However, there was a seasonal variation in the relationship between the PM10 and PM1 extensive properties, as shown in Fig. 6. The seasonal variation in the PM1/PM10 ratio describes the impact of the coarse and fine particles on the σ_{sca} and σ_{abs}.

For the σ_{sca} the seasonal variation in the PM1/PM10 ratio was clear, but for the σ_{abs} there seemed to be no seasonal variation in the ratio whatsoever. The seasonal medians of the PM1/PM10 ration for the σ_{sca} varied from 0.7 to 0.8, and on average submicron particles caused about 75 % of the total scattering of the PM10 particles. This was apparently a lower fraction than in the previous analysis of SMEAR II scattering data. Virkkula et al. (2011) stated that the seasonal average contributions of submicron particles to the total σ_{sca} was in the range of 88–92 %, clearly more than in the present work. However, in that study the scattering size distribution and the contributions of the various size ranges were calculated from particle number size distributions with a Mie model and the physical diameters (D_p) were used whereas here the PM1 corresponds to particles smaller than the aerodynamic diameter D_a of 1 µm. With particle density of 1.7 g cm^{-3} this corresponds to the physical diameter $D_p = (1/1.7)^{½}$ 1 µm ≈ 0.77 µm. The contribution of particles smaller than 0.77 µm is approximately 85 % if it is estimated from Fig. 11 of Virkkula et al. (2011), still more than the ~75 % contribution of submicron scattering shown here. This may have resulted from the cutoff diameter of the PM1 impactor is not exactly sharp and also that the particles entering the impactor may have still been somewhat moist and thus larger than their dry size and were therefore removed from the sample stream. Further analysis of the difference is omitted here.

The maxima of the submicron particle scattering occurred in winter and summer. The summer peak coincided with the maxima of the PM10 α_{sca}, which already indicates that smaller particles play a major role in the size distribution. However, this correlation between the PM1/PM10 ratio and α_{sca} was not observed in winter. In Fig. 2~~Fig. 2~~ (and in Fig. S7), it can be seen that the VMD_{tot} always decreased in the wintertime indicating also the lack of coarse particles. However, on average, the accumulation mode is relatively large compared to the coarse mode and it is shifted towards the larger diameters. This is presented in the supplementary material (Figs. S6 and S7). The large accumulation mode caused α_{sca} to be low, even though there was relatively less scattering by the coarse particles.

For the σ_{abs}, the median of the PM1/PM10 ratio did not greatly vary seasonally. The PM1 particles absorbed about 90 % of the total PM10 particle absorption. So for the σ_{abs} there were no large difference in the σ_{abs} of the PM1 and PM10 particles. The coarse mode particles are typically primary and they have a quite high ω_0 so their absorption is minor compared with the PM1 particles. The soot particles, which account for most of the particulate absorption, are typically submicron particles.

The deviation of the σ_{abs} PM1/PM10 ratio clearly varied seasonally. In summer, the variation was considerably higher than in winter. In the correction algorithm, which was used for the absorption data (Eq. 3), part of the σ_{sca} is subtracted from σ_{abs} as an apparent absorption (Muller et al., 2011). This subtraction causes relatively high uncertainty when the σ_{abs} is low and σ_{sca} is high like it is in summer. This uncertainty is emphasized for PM10 measurements, since the σ_{sca} is relatively higher than σ_{abs} if compared to PM1 measurements. The uncertainty in the measurements also explains why there were so many values above 1 measured in the PM1/PM10 σ_{abs} ratio.

The evolution of the PM1/PM10 ratios were also investigated but we observed no statistically significant trends for either σ_{sca} or σ_{abs}.

3.6 Radiative forcing efficiency

For the aerosol radiative forcing efficiency (RFE) the mean values, trends, and seasonal variation were also investigated. The statistics of the $RFE_{H\&S}$, RFE_S and $RFE_{S,moist}$ are presented in Table 1 and their time series and seasonal variation are presented in Figs. ~~7a and b~~7.

In general, the aerosols, measured at SMEAR II, tend to have a cooling effect on the climate (RFE < 0) as seen in Table 1. By using the global average values suggested by Haywood and Shine (1995), the mean $RFE_{H\&S}$ was -22 Wm^{-2}. This is about 12 % less negative than the mean $RFE_{H\&S}$ (about -25 Wm^{-2}) determined by Sherman et al. (2015) for different North American stations. The difference is explained by higher mean ω_0 (about 0.91) observed by Sherman et al. (2015), the mean b (about 0.14) was similar if compared to average values observed at SMEAR II. Also, a mean $RFE_{H\&S}$ -25 Wm^{-2} was determined at SORPES in China (Shen et al., 2018). Shen et al. (2018) observed a notably higher mean ω_0 (0.93 at 520 nm) than what we observed at SMEAR II (0.87), but for the b the situation was the opposite and it was lower at SORPES (0.12 at 525 nm) than at SMEAR II (0.14 at 550 nm). This would suggest that for dry particles the variation of ω_0 is more pronounced than the variation of b in context of calculating the $RFE_{H\&S}$. This is also observed at SMEAR II (Fig. S9). If the seasonal variation of D, A_C, and R_S were taken into account, the mean RFE_S (-34 Wm^{-2}) was more negative than $RFE_{H\&S}$.

Both, the ω_0 and b tended to increase, which makes the $RFE_{H\&S}$ to decrease (i.e., become more negative). The decreasing $RFE_{H\&S}$ means that the properties of dry aerosol particles have changed so that they cool the climate more efficiently. The trends for the $RFE_{H\&S}$, RFE_S and $RFE_{S,moist}$ are presented in Table 3 as well. Since we used seasonal averages in calculating the RFE_S and $RFE_{S,moist}$, their trends are also depended only on the changes of the ω_0 and b and thus their trends are also decreasing and similar in magnitude as the trend for $RFE_{H\&S}$. However, in reality the trend of RFE does not depend only on the ω_0 and b. For example, a decrease in the snow cover due to global warming would decrease the R_S and make the decrease of RFE steeper. Here, we omitted further analysis on the effect that the changes of A_C, R_S, T_{at} and RH have on the RFE.

The seasonal variation in the $RFE_{H\&S}$ followed the seasonal cycles of the ω_0 and b. The $RFE_{H\&S}$ was minimal in summer and maximal in winter. Since b was lowest (forward-scattering particles) and the ω_0 is also low (dark particles) in winter, the particles clearly did not have as strong a cooling effect as in summer when particles are smaller and light colored. If the seasonal changes of D, A_C, and R_S, were taken into account, the seasonal variability of RFE_S is amplified remarkably compared to $RFE_{H\&S}$ as seen in Fig. 7b. In winter, the D is lower and the A_C is higher, which are shown in Fig. S1, causing the aerosol particles to have less effect (RFE closer to zero) than in summer. During winter the higher R_S causes the aerosol particles to be less cooling or even warming. We chose to use the R_S determined for a boreal forest according to the surroundings of SMEAR II. However, the area around the station consists also of fields and lakes, which in winter, would act as smooth snow fields. Even for snow containing impurities the R_S is notably higher (> 0.7) than R_s for snow covered boreal forest (Warren and Wiscombe, 1980). Using R_S = 0.7 for winter time data, would increase the RFE_S.

Taking the effect of RH into account increases the ω_0 since the aerosols scatter more light due to hygroscopic growth. However, the same effect decreases the b since the particles grow in size and scatter relatively less light backwards (Birmili et al., 2009). The seasonality of RH is presented in Fig. S1d and on average the RH is higher in winter than in summer. Fig. 7b shows that that the $RFE_{S,moist}$ is less negative in summer compared to RFE_S since the effect of RH on b overcomes the effect on ω_0. Fierz-Schmidhauser et al. (2010) also observed this kind of behavior at the Jungfraujoch station. In winter the situation is the opposite and $RFE_{S,moist}$ is more negative than RFE_S. However, in winter, the effect of RH is small due to the small D and large A_C. In general, the observed effect of the RH on RFE is smaller than the effect of taking the seasonal variation of D, A_C, and R_S into account.

The RFE (or $\Delta F\delta^{-1}$) describes only the efficiency of the aerosol particles in cooling or warming the climate per unit of aerosol optical depth (δ). Eq. 13 assumes that the properties of the aerosol particles are uniform in the atmospheric column that is rarely the case in reality. In ambient air, we should also take into account the variability in RH as a function of height. At the top of the boundary layer we typically have RH values close to 100 %. Here, we determined the RFE by using the RH measured near the ground (16 m). The simplified RFE does not give an absolute value for the aerosol forcing; however, it can still indicate how the changes in AOPs affect the climate.

Even if the RFE was very negative, the influence of aerosol particles on the climate would be small if the δ was small. The δ is highly dependent on the σ_{sca} and σ_{abs}; the more there are scattering and absorbing material in the atmosphere, the higher the δ. This is analyzed in further detail in Fig. 8, where the ω_0 is presented as a function of b. In Fig. 8~~Fig. 12~~ the $RFE_{H\&S}$ is presented with isolines and the σ_{sca} is presented by color-coding. Fig. 8~~Figure 12~~ shows that when the $RFE_{H\&S}$ is most negative, the median σ_{sca} is actually experiencing its lowest value. When the $RFE_{H\&S}$ is closest to zero, the median σ_{sca} is the highest. It

is also seen that when the b is high and the particle size distribution consists of smaller particles, the particles are most efficient at cooling the atmosphere even though the average ω_0 is the lowest.

These relationships were also observed in a study of AOPs at the Station for Observing Regional Processes of the Earth System (SORPES), a measurement station in Nanjing China (Shen et al., 2018). Also, Delene and Ogren (2002) and Sherman et al. (2015) observed similar systematic variability between σ_{sca}, ω_0, b, and $RFE_{H\&S}$ at several North American measurement stations; when the σ_{sca} increases, the ω_0 increases and the b decreases. Sherman et al. (2015) suggested that this variability could be caused by deposition of larger particles, which typically absorb less light. Delene and Ogren (2002) observed that $RFE_{H\&S}$ increases (i.e. becomes less negative) with increasing σ_{sca}, but Sherman et al. (2015) did not observe this trend.

4 Summary and c~~C~~onclusions

In this study, we presented over 11-year long time series of AOPs measured at SMEAR II, a station in southern Finland. With the long time series, it was possible to see statistically significant trends, seasonal variation, and different types of causalities between the optical properties. We compared the AOPs with the aerosol size distribution measurements conducted at the station and observed in detail how the AOPs are dependent on the shape of the size distribution. By comparing the AOPs and size distribution, we were able to determine the m values that can be used in modeling the σ_{sca} and σ_{abs} from size distribution measurements.

The extensive AOPs, as well as the aerosol number and volume concentration, tended to decrease. Our observation was in line with the other studies conducted in Europe and North America that also observed decreasing trends for the extensive AOPs (Collaud Coen et al., 2013; Pandolfi et al., 2018; Sherman et al., 2015), number concentration (Asmi et al., 2013) and aerosol optical depth (Li et al., 2014). This uniform decreasing trend in the amount of aerosol particles suggests that the anthropogenic emissions of particulate matter and gases that take part in secondary aerosol formation has been decreasing in Europe and North America.~~.~~ The observed tendency for b and α_{sca} to increase together with the decreasing extensive properties indicated that the particle size distribution ~~was moving towards~~consisted of less larger particles ~~smaller diameters~~. A more detailed investigation revealed that the number of larger accumulation mode particles decreased relatively the fastest, which also supports the assumed decrease in pollution.

There ~~are~~ were clear~~ly~~ seasonal variations in the AOPs. The largest differences occur during summer and winter. The seasonal variations in the extensive properties ~~and~~, ω_0 and size distribution revealed that in winter the particles have a larger contribution from the anthropogenic sources than during summer.

Since the aerosol particles are smaller and less dark than before, their RFE tended to decrease (i.e. became more negative), which means that the ability of aerosols to cool the climate per unit δ increased. However, since the extensive properties and particle number concentration are decreasing, which means that the δ decreases as well, the total aerosol forcing is probably also decreasing. We determined the RFE to dry aerosol particles by using global average values suggested by Haywood and Shine (1995). To test the sensitivity of RFE to environmental parameters (D, R_S, and A_C), we calculated the RFE also by using more realistic and seasonally averaged environmental parameters. We also determined the RFE for ambient RH, since it is affected by the hygroscopic growth of aerosols. We observed that at SMEAR II the environmental parameters had a higher impact on the RFE than the ambient RH. Here we only studied the effect of AOPs on the RFE. Taking the long-term trend of environmental parameters into account would probably have a large effect on the trend of the RFE.

Data availability

All the data presented in this study is open access. The optical properties and the size distribution data from SMEAR II has been uploaded on the EBAS database (EBAS: http://ebas.nilu.no/, last access: 18 March 2019) run by the Norwegian Institute for Air Research (NILU). Meteorological parameters measured at SMEAR II, such as the RH used here, can be accessed by the Smart-SMEAR online tool (Junninen et al., 2009). Also the Finnish Meteorological Institute provides open access data and we used their online data tool (FMI: https://ilmatieteenlaitos.fi/havaintojen-lataus, last access: 18 March 2019) to access the ceilometer data measured at Halli airport.

References

Aalto, P., Hämeri, K., Becker, E., Weber, R., Salm, J., Mäkelä, J. M., Hoell, C., O'dowd, C. D., Hansson, H.-C., and Väkevä, M.: Physical characterization of aerosol particles during nucleation events, Tellus B: Chemical and Physical Meteorology, 53, 344-358, 2001.

Anderson, T. L., and Ogren, J. A.: Determining aerosol radiative properties using the TSI 3563 integrating nephelometer, Aerosol Science and Technology, 29, 57-69, 1998.

Andrews, E., Ogren, J., Bonasoni, P., Marinoni, A., Cuevas, E., Rodríguez, S., Sun, J. Y., Jaffe, D., Fischer, E., and Baltensperger, U.: Climatology of aerosol radiative properties in the free troposphere, Atmospheric Research, 102, 365-393, 2011.

Arnott, W. P., Hamasha, K., Moosmüller, H., Sheridan, P. J., and Ogren, J. A.: Towards aerosol light-absorption measurements with a 7-wavelength aethalometer: Evaluation with a photoacoustic instrument and 3-wavelength nephelometer, Aerosol Science and Technology, 39, 17-29, 2005.

Asmi, A., Collaud Coen, M., Ogren, J., Andrews, E., Sheridan, P., Jefferson, A., Weingartner, E., Baltensperger, U., Bukowiecki, N., and Lihavainen, H.: Aerosol decadal trends–Part 2: In-situ aerosol particle number concentrations at GAW and ACTRIS stations, Atmospheric Chemistry and Physics, 13, 895-916, 2013.

Backman, J., Schmeisser, L., Virkkula, A., Ogren, J. A., Asmi, E., Starkweather, S., Sharma, S., Eleftheriadis, K., Uttal, T., and Jefferson, A.: On Aethalometer measurement uncertainties and an instrument correction factor for the Arctic, Atmospheric Measurement Techniques, 2017.

Bergin, M. H., Ogren, J. A., Schwartz, S. E., and McInnes, L. M.: Evaporation of ammonium nitrate aerosol in a heated nephelometer: Implications for field measurements, Environmental Science & Technology, 31, 2878-2883, 1997.

Birmili, W., Schwirn, K., Nowak, A., Petäjä, T., Joutsensaari, J., Rose, D., Wiedensohler, A., Hämeri, K., Aalto, P., and Kulmala, M.: Measurements of humidified particle number size distributions in a Finnish boreal forest: derivation of hygroscopic particle growth factors, Boreal Environment Research, 14, 458-480, 2009.

Boucher, O., Randall, D., Artaxo, P., Bretherton, C., Feingold, G., Forster, P., Kerminen, V.-M., Kondo, Y., Liao, H., and Lohmann, U.: Clouds and aerosols, in: Climate Change 2013: the physical science basis. Contribution of Working Group I to the Fifth Assessment Report of the Intergovernmental Panel on Climate Change, Cambridge University Press, 571-657, 2013.

Casati, R., Scheer, V., Vogt, R., and Benter, T.: Measurement of nucleation and soot mode particle emission from a diesel passenger car in real world and laboratory in situ dilution, Atmospheric Environment, 41, 2125-2135, 2007.

Charlson, R. J., Schwartz, S., Hales, J., Cess, R. D., Coakley, J. J., Hansen, J., and Hofmann, D.: Climate forcing by anthropogenic aerosols, Science, 255, 423-430, 1992.

Collaud Coen, M., Weingartner, E., Nyeki, S., Cozic, J., Henning, S., Verheggen, B., Gehrig, R., and Baltensperger, U.: Long-term trend analysis of aerosol variables at the high-alpine site Jungfraujoch, Journal of Geophysical Research: Atmospheres, 112, 2007.

Collaud Coen, M., Weingartner, E., Apituley, A., Ceburnis, D., Fierz-Schmidhauser, R., Flentje, H., Henzing, J., Jennings, S. G., Moerman, M., and Petzold, A.: Minimizing light absorption measurement artifacts of the Aethalometer: evaluation of five correction algorithms, Atmospheric Measurement Techniques, 3, 457-474, 2010.

Collaud Coen, M., Andrews, E., Asmi, A., Baltensperger, U., Bukowiecki, N., Day, D., Fiebig, M., Fjæraa, A. M., Flentje, H., and Hyvärinen, A.: Aerosol decadal trends–Part 1: In-situ optical measurements at GAW and IMPROVE stations, Atmospheric Chemistry and Physics, 13, 869-894, 2013.

Dal Maso, M., Kulmala, M., Riipinen, I., Wagner, R., Hussein, T., Aalto, P. P., and Lehtinen, K. E.: Formation and growth of fresh atmospheric aerosols: eight years of aerosol size distribution data from SMEAR II, Hyytiala, Finland, Boreal Environment Research, 10, 323-336, 2005.

Delene, D. J., and Ogren, J. A.: Variability of aerosol optical properties at four North American surface monitoring sites, Journal of the Atmospheric Sciences, 59, 1135-1150, 2002.

Ehn, M., Thornton, J. A., Kleist, E., Sipilä, M., Junninen, H., Pullinen, I., Springer, M., Rubach, F., Tillmann, R., and Lee, B.: A large source of low-volatility secondary organic aerosol, Nature, 506, 476, 2014.

Fierz-Schmidhauser, R., Zieger, P., Gysel, M., Kammermann, L., DeCarlo, P., Baltensperger, U., and Weingartner, E.: Measured and predicted aerosol light scattering enhancement factors at the high alpine site Jungfraujoch, Atmospheric Chemistry and Physics, 10, 2319-2333, 2010.

Garland, R., Yang, H., Schmid, O., Rose, D., Nowak, A., Achtert, P., Wiedensohler, A., Takegawa, N., Kita, K., and Miyazaki, Y.: Aerosol optical properties in a rural environment near the mega-city Guangzhou, China: implications for regional air pollution, radiative forcing and remote sensing, Atmospheric Chemistry and Physics, 8, 5161-5186, 2008.

Gilbert, R. O.: Statistical methods for environmental pollution monitoring, John Wiley & Sons, 1987.

Gyawali, M., Arnott, W., Lewis, K., and Moosmüller, H.: In situ aerosol optics in Reno, NV, USA during and after the summer 2008 California wildfires and the influence of absorbing and non-absorbing organic coatings on spectral light absorption, Atmospheric Chemistry and Physics, 9, 8007-8015, 2009.

Hari, P., and Kulmala, M.: Station for Measuring Ecosystem–Atmosphere Relations, Boreal Environment Research, 10, 315-322, 2005.

Hari, P., Nikinmaa, E., Pohja, T., Siivola, E., Bäck, J., Vesala, T., and Kulmala, M.: Station for measuring ecosystem-atmosphere relations: SMEAR, in: Physical and Physiological Forest Ecology, Springer, 471-487, 2013.

Haywood, J., and Shine, K.: The effect of anthropogenic sulfate and soot aerosol on the clear sky planetary radiation budget, Geophysical Research Letters, 22, 603-606, 1995.

Haywood, J., and Boucher, O.: Estimates of the direct and indirect radiative forcing due to tropospheric aerosols: A review, Reviews of Geophysics, 38, 513-543, 2000.

Hienola, A., Pietikäinen, J.-P., Jacob, D., Pozdun, R., Petäjä, T., Hyvärinen, A.-P., Sogacheva, L., Kerminen, V.-M., Kulmala, M., and Laaksonen, A.: Black carbon concentration and deposition estimations in Finland by the regional aerosol-climate model REMO-HAM, Atmospheric Chemistry and Physics, 13, 4033, 2013.

Hyvärinen, A.-P., Kolmonen, P., Kerminen, V.-M., Virkkula, A., Leskinen, A., Komppula, M., Hatakka, J., Burkhart, J., Stohl, A., and Aalto, P.: Aerosol black carbon at five background measurement sites over Finland, a gateway to the Arctic, Atmospheric Environment, 45, 4042-4050, 2011.

Junninen, H., Lauri, A., Keronen, P., Aalto, P., Hiltunen, V., Hari, P., and Kulmala, M.: Smart-SMEAR: on-line data exploration and visualization tool for SMEAR stations, Boreal Environment Research, 14, 447-457, 2009.

Karvosenoja, N., Kangas, L., Kupiainen, K., Kukkonen, J., Karppinen, A., Sofiev, M., Tainio, M., Paunu, V.-V., Ahtoniemi, P., and Tuomisto, J. T.: Integrated modeling assessments of the population exposure in Finland to primary PM2. 5 from traffic and domestic wood combustion on the resolutions of 1 and 10 km, Air Quality, Atmosphere & Health, 4, 179-188, 2011.

Kittelson, D. B.: Engines and nanoparticles: a review, Journal of Aerosol Science, 29, 575-588, 1998.

Kulmala, M., Vehkamäki, H., Petäjä, T., Dal Maso, M., Lauri, A., Kerminen, V.-M., Birmili, W., and McMurry, P.: Formation and growth rates of ultrafine atmospheric particles: a review of observations, Journal of Aerosol Science, 35, 143-176, 2004.

Kulmala, M., Kontkanen, J., Junninen, H., Lehtipalo, K., Manninen, H. E., Nieminen, T., Petäjä, T., Sipilä, M., Schobesberger, S., and Rantala, P.: Direct observations of atmospheric aerosol nucleation, Science, 339, 943-946, 2013.

Kulmala, M., Luoma, K., Virkkula, A., Petäjä, T., Paasonen, P., Kerminen, V.-M., Nie, W., Qi, X., Shen, Y., and Chi, X.: On the mode-segregated aerosol particle number concentration load: contributions of primary and secondary particles in Hyytiälä and Nanjing, Boreal Environment Research, 21, 319-331, 2016.

Kuusinen, N., Kolari, P., Levula, J., Porcar-Castell, A., Stenberg, P., and Berninger, F.: Seasonal variation in boreal pine forest albedo and effects of canopy snow on forest reflectance, Agricultural and Forest Meteorology, 164, 53-60, 2012.

Lack, D., and Cappa, C.: Impact of brown and clear carbon on light absorption enhancement, single scatter albedo and absorption wavelength dependence of black carbon, Atmospheric Chemistry and Physics, 10, 4207-4220, 2010.

Leskinen, A., Arola, A., Komppula, M., Portin, H., Tiitta, P., Miettinen, P., Romakkaniemi, S., Laaksonen, A., and Lehtinen, K.: Seasonal cycle and source analyses of aerosol optical properties in a semi-urban environment at Puijo station in Eastern Finland, Atmospheric Chemistry and Physics, 12, 5647, 2012.

Li, J., Carlson, B. E., Dubovik, O., and Lacis, A. A.: Recent trends in aerosol optical properties derived from AERONET measurements, Atmospheric Chemistry and Physics, 14, 12271-12289, 2014.

Lihavainen, H., Hyvärinen, A., Asmi, E., Hatakka, J., and Viisanen, Y.: Long-term variability of aerosol optical properties in northern Finland, Boreal Environment Research, 20, 526-541, 2015.

Lohmann, U., and Feichter, J.: Impact of sulfate aerosols on albedo and lifetime of clouds: A sensitivity study with the ECHAM4 GCM, Journal of Geophysical Research: Atmospheres, 102, 13685-13700, 1997.

Muller, T., Henzing, J., De Leeuw, G., Wiedensohler, A., Alastuey, A., Angelov, H., Bizjak, M., Coen, M., Engstrom, J., and Gruening, C.: Characterization and intercomparison of aerosol absorption photometers: result of two intercomparison workshops, Atmospheric Measurement Techniques, 4, 245-268, 2011.

Mätzler, C.: MATLAB functions for Mie scattering and absorption, version 2, Institut für Angewandte Physik, University of Bern, 2002.

Nessler, R., Weingartner, E., and Baltensperger, U.: Effect of humidity on aerosol light absorption and its implications for extinction and the single scattering albedo illustrated for a site in the lower free troposphere, Journal of Aerosol Science, 36, 958-972, 2005.

Pandolfi, M., Alados-Arboledas, L., Alastuey, A., Andrade, M., Angelov, C., Artiñano, B., Backman, J., Baltensperger, U., Bonasoni, P., and Bukowiecki, N.: A European aerosol phenomenology–6: scattering properties of atmospheric aerosol particles from 28 ACTRIS sites, Atmospheric Chemistry and Physics, 18, 7877-7911, 2018.

Saarikoski, S., Makela, T., Hillamo, R., Aalto, P. P., Kerminen, V., and Kulmala, M.: Physico-chemical characterization and mass closure of size-segregated atmospheric aerosols in Hyytiala, Finland, Boreal Environment Research, 10, 385-400, 2005.

Sandradewi, J., Prévôt, A. S., Szidat, S., Perron, N., Alfarra, M. R., Lanz, V. A., Weingartner, E., and Baltensperger, U.: Using aerosol light absorption measurements for the quantitative determination of wood burning and traffic emission contributions to particulate matter, Environmental Science & Technology, 42, 3316-3323, 2008.

Schnaiter, M., Linke, C., Möhler, O., Naumann, K. H., Saathoff, H., Wagner, R., Schurath, U., and Wehner, B.: Absorption amplification of black carbon internally mixed with secondary organic aerosol, Journal of Geophysical Research: Atmospheres, 110, 2005.

Schuster, G. L., Dubovik, O., and Holben, B. N.: Angstrom exponent and bimodal aerosol size distributions, Journal of Geophysical Research: Atmospheres, 111, 2006.

Shen, Y., Virkkula, A., Ding, A., Wang, J., Chi, X., Nie, W., Qi, X., Huang, X., Liu, Q., and Zheng, L.: Aerosol optical properties at SORPES in Nanjing, east China, Atmospheric Chemistry and Physics, 18, 5265-5292, 2018.

Sheridan, P. J., and Ogren, J. A.: Observations of the vertical and regional variability of aerosol optical properties over central and eastern North America, Journal of Geophysical Research: Atmospheres, 104, 16793-16805, 1999.

Sherman, J., Sheridan, P., Ogren, J., Andrews, E., Hageman, D., Schmeisser, L., Jefferson, A., and Sharma, S.: A multi-year study of lower tropospheric aerosol variability and systematic relationships from four North American regions, Atmospheric Chemistry and Physics, 15, 12487-12517, 2015.

Tunved, P., Hansson, H.-C., Kerminen, V.-M., Ström, J., Dal Maso, M., Lihavainen, H., Viisanen, Y., Aalto, P., Komppula, M., and Kulmala, M.: High natural aerosol loading over boreal forests, Science, 312, 261-263, 2006.

Twomey, S.: Aerosols, clouds and radiation, Atmospheric Environment, 25A, 2435-2442, 1991.

Tørseth, K., Aas, W., Breivik, K., Fjæraa, A. M., Fiebig, M., Hjellbrekke, A.-G., Lund Myhre, C., Solberg, S., and Yttri, K. E. J. A. C.: Introduction to the European Monitoring and Evaluation Programme (EMEP) and observed atmospheric composition change during 1972–2009, Atmospheric Chemistry and Physics, 12, 5447-5481, 2012.

Warren, S. G., and Wiscombe, W. J. J. J. o. t. A. S.: A model for the spectral albedo of snow. II: Snow containing atmospheric aerosols, 37, 2734-2745, 1980.

Virkkula, A., Backman, J., Aalto, P., Hulkkonen, M., Riuttanen, L., Nieminen, T., Dal Maso, M., Sogacheva, L., De Leeuw, G., and Kulmala, M.: Seasonal cycle, size dependencies, and source analyses of aerosol optical properties at the SMEAR II measurement station in Hyytiala, Finland, Atmospheric Chemistry and Physics, 11, 4445, 2011.

WMO/GAW: Aerosol Measurement Procedures, Guidelines and Recommendations, GAW Report No. 153, World Meteorological Organization, Geneva, Switzerland, 2003.

WMO/GAW: Aerosol Measurement Procedures, Guidelines and Recommendations, 2nd edition, GAW Report No. 227, World Meteorological Organization, Geneva, Switzerland, 2016.

Zhang, R., Khalizov, A. F., Pagels, J., Zhang, D., Xue, H., and McMurry, P. H.: Variability in morphology, hygroscopicity, and optical properties of soot aerosols during atmospheric processing, Proceedings of the National Academy of Sciences, 105, 10291-10296, 2008.

Zieger, P., Aalto, P., Aaltonen, V., Äijälä, M., Backman, J., Hong, J., Komppula, M., Krejci, R., Laborde, M., and Lampilahti, J.: Low hygroscopic scattering enhancement of boreal aerosol and the implications for a columnar optical closure study, Atmospheric Chemistry and Physics, 15, 7247-7267, 2015.

Zotter, P., Herich, H., Gysel, M., El-Haddad, I., Zhang, Y., Močnik, G., Hüglin, C., Baltensperger, U., Szidat, S., and Prévôt, A. S.: Evaluation of the absorption Ångström exponents for traffic and wood burning in the Aethalometer-based source apportionment using radiocarbon measurements of ambient aerosol, Atmospheric Chemistry and Physics, 17, 4229-4249, 2017.

Ångström, A.: On the atmospheric transmission of sun radiation and on dust in the air, Geografiska Annaler, 11, 156-166, 1929.

Table 1: Average values of the AOPs for the PM10 particles. The average values were calculated from all valid data.

PM10	λ (nm)	mean ± SD	1 %	10 %	25 %	50 %	75 %	90 %	99 %
σ_{sca} (Mm^{-1})	450	21.8 ± 23.3	1.8	4.5	7.6	14.2	26.8	48.5	114.1
	550	15.2 ± 16.7	1.3	3.4	5.5	9.8	18.3	33.4	82.5
	700	9.5 ± 10.5	0.8	2.3	3.7	6.3	11.3	20.3	52.3
σ_{bsca} (Mm^{-1})	450	2.5 ± 2.9	0.2	0.6	1.0	1.8	3.2	5.3	11.1
	550	2.0 ± 1.8	0.2	0.5	0.8	1.4	2.5	4.2	8.8
	700	1.6 ± 1.5	0.2	0.4	0.7	1.2	2.0	3.4	7.4
σ_{abs} (Mm^{-1})	370	3.0 ± 3.6	0.2	0.6	1.0	1.9	3.6	6.6	18.1
	470	2.5 ± 2.9	0.2	0.5	0.8	1.6	3.0	5.4	14.3
	520	2.2 ± 2.4	0.1	0.4	0.7	1.4	2.6	4.7	12.3
	590	1.9 ± 2.2	0.1	0.4	0.7	1.3	2.4	4.2	10.8
	660	1.8 ± 2.0	0.1	0.3	0.6	1.2	2.2	3.8	9.9
	880	1.3 ± 1.4	0.1	0.3	0.5	0.9	1.6	2.9	7.2
	950	1.2 ± 1.3	0.1	0.3	0.4	0.8	1.5	2.6	6.5
ω_0	450	0.88 ± 0.07	0.64	0.80	0.85	0.89	0.93	0.95	0.98
	550	0.87 ± 0.07	0.62	0.78	0.84	0.88	0.92	0.94	0.98
	700	0.84 ± 0.08	0.55	0.74	0.80	0.85	0.90	0.93	0.97
b	450	0.13 ± 0.03	0.08	0.10	0.11	0.12	0.14	0.16	0.21
	550	0.14 ± 0.03	0.09	0.11	0.13	0.14	0.16	0.17	0.21
	700	0.19 ± 0.07	0.07	0.13	0.15	0.18	0.21	0.25	0.44
α_{sca}	450/550	1.73 ± 0.52	0.23	1.03	1.49	1.82	2.09	2.29	2.58
	450/700	1.80 ± 0.55	0.32	1.00	1.53	1.88	2.17	2.39	2.80
	550/700	1.85 ± 0.64	0.23	0.95	1.53	1.95	2.26	2.50	3.15
α_{abs}	370/520	0.95 ± 0. 48	-0.29	0.51	0.76	0.98	1.16	1.32	1.97
	370/950	0.95 ± 0.36	-0.16	0.55	0.80	0.99	1.13	1.24	1.69
	470/660	0.95 ± 0.49	-0.52	0.52	0.80	1.01	1.15	1.29	2.07
	470/950	0.99 ± 0.41	-0.32	0.58	0.86	1.06	1.18	1.28	1.83
	660/950	1.02 ± 0.57	-0.77	0.57	0.90	1.11	1.23	1.34	2.17
n	450	1.541 ± 0.065	1.330	1.478	1.512	1.542	1.572	1.607	1.697
	550	1.518 ± 0.067	1.289	1.452	1.490	1.522	1.550	1.581	1.674
	700	1.491 ± 0.091	1.247	1.379	1.454	1.501	1.536	1.574	1.740
k	450	0.021 ± 0.020	0.002	0.006	0.009	0.016	0.026	0.039	0.097
	550	0.020 ± 0.018	0.002	0.006	0.010	0.016	0.025	0.038	0.089
	700	0.022 ± 0.019	0.003	0.007	0.011	0.018	0.027	0.041	0.092
$RFE_{H\&S}$ (Wm^{-2})	550	-22 ± 6	-32	-28	-26	-23	-19	-16	-3
RFE_{S} (Wm^{-2})	550	-35 ± 32	-97	-82	-67	-26	-5	0	12
$RFE_{S,moist}$ (Wm^{-2})	550	-32 ± 28	-85	-72	-60	-24	-5	-2	5

Table 2: Average values of the AOPs for the PM1 particles. The average values were calculated from all valid data; th~~us~~erefore if compared with the PM10 average values, there is a 4-year shorter dataset.

PM1	λ (nm)	mean ± SD	1 %	10 %	25 %	50 %	75 %	90 %	99 %
σ_{sca} (Mm^{-1})	450	17.7 ± 19.2	1.2	3.1	5.6	11.3	22.3	40.4	96.1
	550	11.4 ± 13.0	0.8	2.1	3.6	7.1	14.1	26.1	64.8
	700	6.3 ± 7.5	0.4	1.2	2.0	3.8	7.6	14.4	37.4
σ_{bsca} (Mm^{-1})	450	2.1 ± 2.0	0.2	0.4	0.8	1.4	2.7	4.5	9.7
	550	1.6 ± 1.5	0.1	0.3	0.6	1.1	2.0	3.4	7.5
	700	1.2 ± 1.2	0.1	0.3	0.5	0.8	1.5	2.6	5.9
σ_{abs} (Mm^{-1})	370	2.4 ± 2.9	0.1	0.4	0.8	1.6	2.9	5.2	15.0
	470	2.0 ± 2.3	0.1	0.4	0.7	1.3	2.4	4.3	11.7
	520	1.7 ± 1.9	0.1	0.3	0.6	1.2	2.1	3.7	10.0
	590	1.6 ± 1.7	0.1	0.3	0.5	1.0	1.9	3.3	8.8
	660	1.4 ± 1.6	0.1	0.3	0.5	01.0	1.8	3.1	8.0
	880	1.1 ± 1.1	0.1	0.2	0.4	0.7	1.3	2.3	5.8
	950	0.9 ± 1.0	0.0	0.2	0.3	0.6	1.2	2.0	5.1
ω_0	450	0.88 ± 0.08	0.62	0.78	0.84	0.89	0.93	0.96	0.98
	550	0.85 ± 0.08	0.59	0.75	0.81	0.87	0.91	0.94	0.98
	700	0.80 ± 0.10	0.48	0.67	0.75	0.81	0.87	0.91	0.96
b	450	0.13 ± 0.03	0.07	0.10	0.11	0.13	0.14	0.17	0.23
	550	0.15 ± 0.03	0.09	0.12	0.13	0.15	0.17	0.19	0.24
	700	0.23 ± 0.13	-0.06	0.14	0.17	0.21	0.26	0.34	0.78
α_{sca}	450/700	2.22 ± 0.44	0.88	1.70	1.99	2.28	2.51	2.66	2.95
	450/550	2.36 ± 0.55	0.74	1.76	2.09	2.41	2.66	2.87	3.70
	550/700	2.48 ± 0.81	0.25	1.73	2.16	2.52	2.82	3.13	4.69
α_{abs}	370/520	0.96 ± 0.61	-0.67	0.47	0.74	0.99	1.20	1.39	2.32
	370/950	0.97 ± 0.44	-0.36	0.52	0.80	1.03	1.19	1.33	1.96
	470/660	0.94 ± 0.66	-0.94	0.46	0.76	1.00	1.17	1.33	2.35
	470/950	1.03 ± 0.51	-0.51	0.56	0.87	1.11	1.25	1.39	2.24
	660/950	1.13 ± 0.72	-1.10	0.60	0.97	1.20	1.35	1.54	2.96
n	450	1.509 ± 0.057	1.348	1.441	1.478	1.513	1.542	1.568	1.634
	550	1.484 ± 0.054	1.338	1.422	1.456	1.487	1.516	1.540	1.598
	700	1.471 ± 0.074	1.294	1.393	1.435	1.472	1.505	1.537	1.677
k	450	0.025 ± 0.020	0.003	0.008	0.013	0.020	0.031	0.045	0.099
	550	0.025 ± 0.018	0.004	0.009	0.014	0.021	0.031	0.044	0.093
	700	0.028 ± 0.019	0.005	0.011	0.017	0.024	0.035	0.049	0.098

Table 3: Slopes of the trends (in absolute values and in estimated percentages per year) and their statistical significance. The lower and upper limits in the 95 % confidence interval for different optical properties are also shown. The trend in the percentage was determined by comparing the slope of the trend with the overall median of the data.

		PM10					PM1				
	λ (nm)	Trend (yr^{-1})		Lower (yr^{-1})	Upper (yr^{-1})	*p*-value	Trend (yr^{-1})		Lower (yr^{-1})	Upper (yr^{-1})	*p*-value
σ_{sca} (Mm^{-1})	550	-0.32	-3 %	-0.52	-0.17	< 0.01	-0.30	-4 %	-0.55	-0.12	< 0.01
σ_{bsca} (Mm^{-1})	550	-0.038	-3 %	-0.070	-0.021	< 0.01	-0.051	-5 %	-0.087	-0.013	< 0.01
σ_{abs} (Mm^{-1})	520	-0.086	-6 %	-0.133	-0.044	< 0.01	-0.141	-12 %	-0.166	-0.098	< 0.01
ω_0	550	2.2e-3	0.3 %	0.7e-3	3.6e-3	< 0.01	5.5e-3	0.6 %	1.5e-3	10e-3	< 0.01
b	550	1.3e-3	0.9 %	0.9e-3	1.7e-3	< 0.01	1.5e-3	1 %	0.7e-3	2.6e-3	< 0.01
α_{sca}	450/700	0.012	0.7 %	-0.001	0.024	0.07	0.014	0.6 %	0.004	0.024	< 0.01
α_{abs}	370/950	-1.5e-4	0 %	-3.0e-3	2.9e-5	0.95	-3.5e-3	-0.3 %	-7.9e-3	13e-3	0.34
n	550	-2.0e-3	-0 %	-3.8e-3	0.6e-3	0.11	-5.7e-3	-0.4 %	-7.5e-3	-2.9e-3	< 0.01
k	550	-6.6e-4	-4 %	-9.1e-4	-3.8e-4	< 0.01	-1.3e-3	-6 %	-2.0e-3	-0.7e-3	< 0.01
$RFE_{H\&S}$ (Wm^{-2})	550	-0.30	-1 %	-0.43	-0.20	< 0.01					
RFE_{S} (Wm^{-2})	550	-0.43	-2 %	-0.64	-0.25	< 0.01					
$RFE_{S,moist}$ (Wm^{-2})	550	-0.39	-2 %	-0.50	-24	< 0.01					
N_{tot} (cm^{-3})		-40	-3 %	-52	-28	< 0.01					
V_{tot} (µg cm^{-3})		-0.093	-4 %	-0.120	-0.064	< 0.01					
VMD_{tot} (nm)		-12	-1 %	-17	-7	< 0.01					

Table 4: Slopes of the seasonal trends and their statistical significance for σ_{sca} and σ_{abs}. The trend in the percentage was determined by comparing the slope of the trend with the seasonal median of the data.

	σ_{sca} (Mm^{-1})					σ_{abs} (Mm^{-1})				
	Trend (yr^{-1})		Lower (yr^{-1})	Upper (yr^{-1})	*p*-value	Trend (yr^{-1})		Lower (yr^{-1})	Upper (yr^{-1})	*p*-value
Spring	-0.44	-5 %	-0.84	-0.04	< 0.05	-0.12	-9 %	-0.20	-0.05	< 0.01
Summer	-0.38	-3 %	-0.79	-0.14	< 0.01	-0.06	-5 %	-0.11	-0.03	< 0.01
Autumn	-0.12	-1 %	-0.49	0.17	0.48	-0.04	-3 %	-0.10	0.03	0.14
Winter	-0.85	-7 %	-1.60	-0.20	< 0.01	-0.17	-8 %	-0.31	-0.03	< 0.05

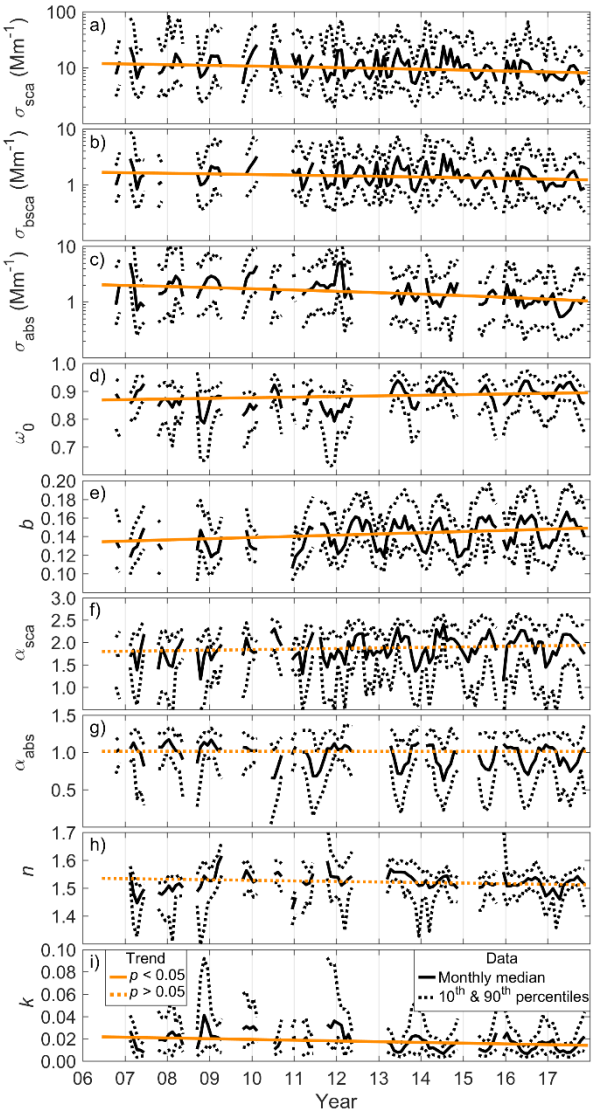

Figure 1: Time series of the AOPs. The uniform black line presents the monthly median and the dotted black lines present the monthly 10th and 90th percentiles. The trends (see Table 3) of the AOPs are shown with orange lines. If the trend was statistically significant, the line is uniform and if the *p*-value of the trend was > 0.05, the line is dashed.

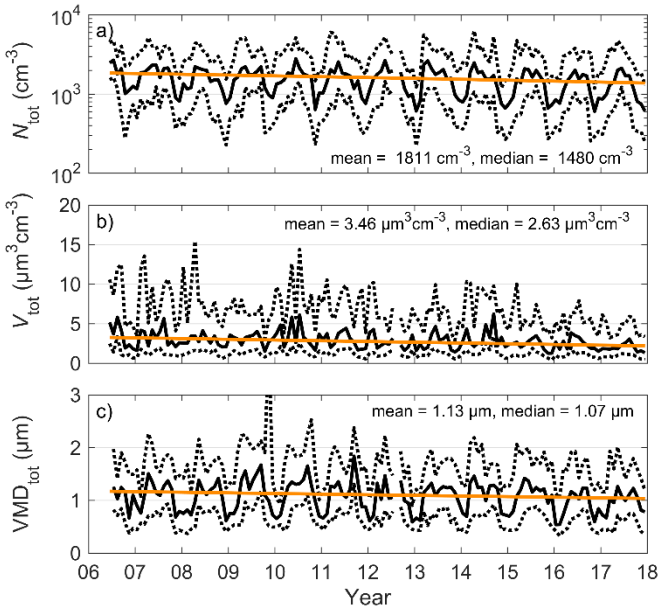

Figure 2: Time series and trends of the total particle (D_p < 10 µm) a) number concentration (N_{tot}), b) volume (V_{tot}) and c) VMD_{tot}. The mean and median values of the variables are also marked in the subfigures and the statistics of their slopes are presented in Table 3. The explanations for the different lines are the same as in Fig. 1 ~~Fig. 1~~.

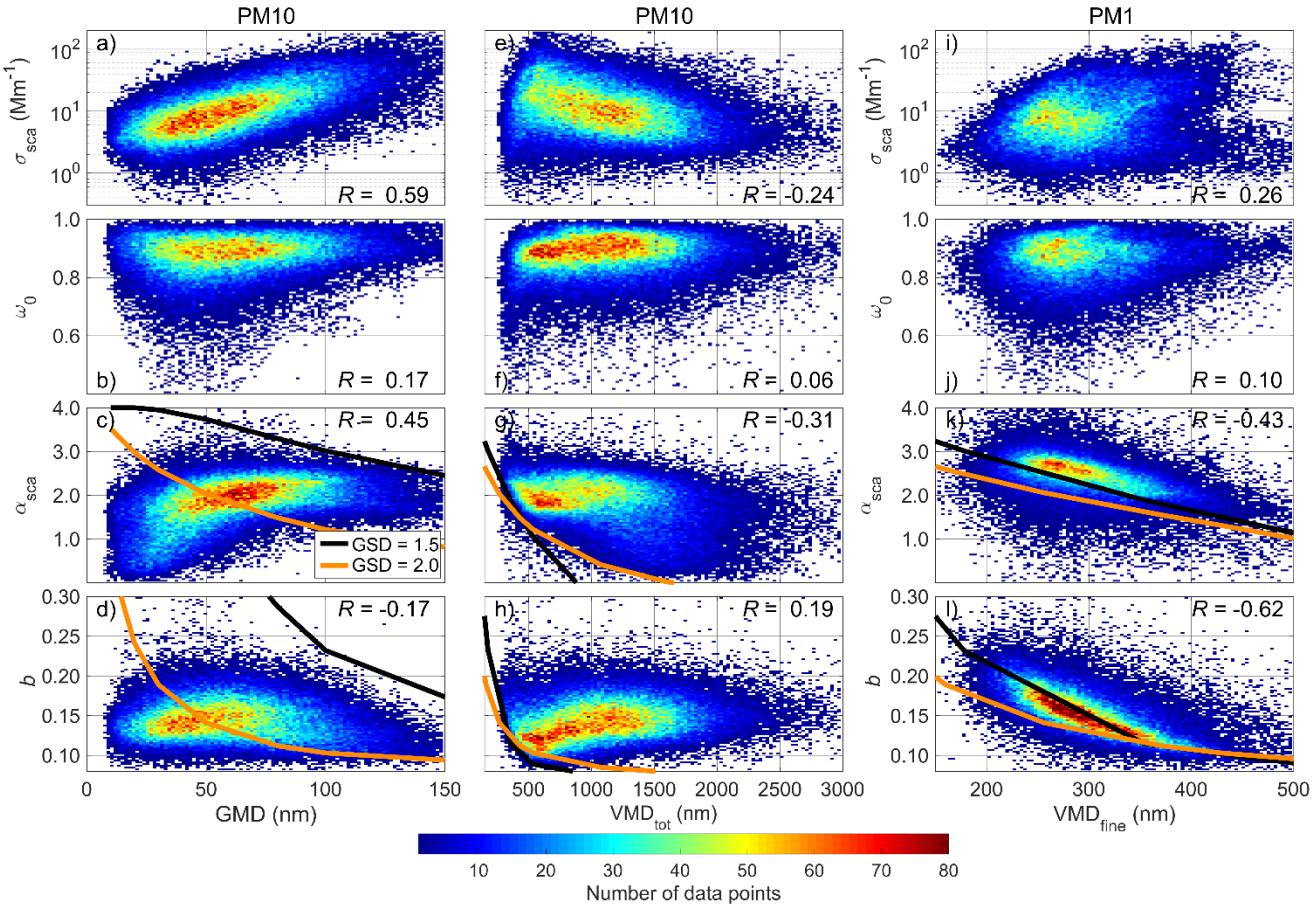

Figure 3: Relationships between the various AOPs, GMD and VMD. Subplots a) – d) describe the correlation between the PM10 AOPs and GMD; subplots e) – h) describe the correlation between the PM10 AOPs and VMD_{tot}; and the subplots i) – l) describe the correlation between the PM1 AOPs and VMD_{fine}. The correlation coefficients of the linear regressions are given in each subfigure. The color-coding represents the number of data points in a grid point. In each subfigure, there are 100 grid points on both axes, making 10 000 grid points in total. The orange and black lines represent the values calculated from the unimodal size distributions, which were generated for different GMDs with geometric standard deviation GSD = 2.0 and 1.5 nm. The scattering was modeled from the generated size distribution at wavelengths 450, 550, and 700 nm with a refractive index *m* = 1.517 + 0.19i.

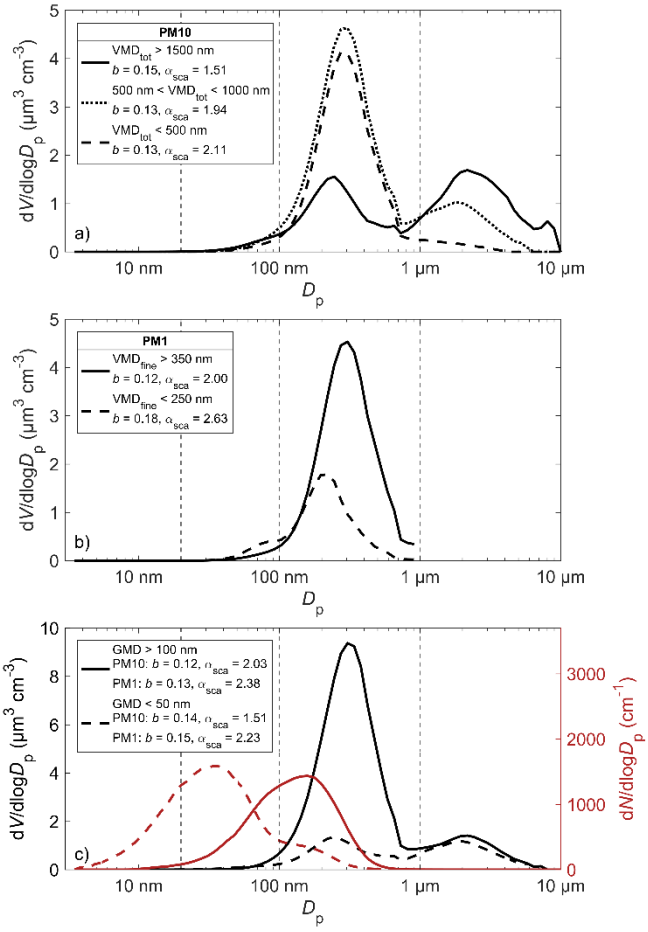

Figure 4: Median volume and number size distributions for the various VMD and GMD limits. The median *b* and α_{sca} for the VMD and GMD limits are given in each legend box. The vertical grid lines represent the typical diameter limits for the nucleation, Aitken, accumulation and coarse particle modes (same as in Figs. S4 and S6 ~~Fig. 3~~). a) Volume size distribution for different PM10 VMD_{tot} limits. b) Volume size distribution for different PM1 VMD_{fine} limits. c) Volume and number size distribution for different PM10 and GMD limits. The c) subfigure also represents volume and number size distribution for different PM1 and GMD limits as well, since the GMD is practically the same for PM10 and PM1 particles.

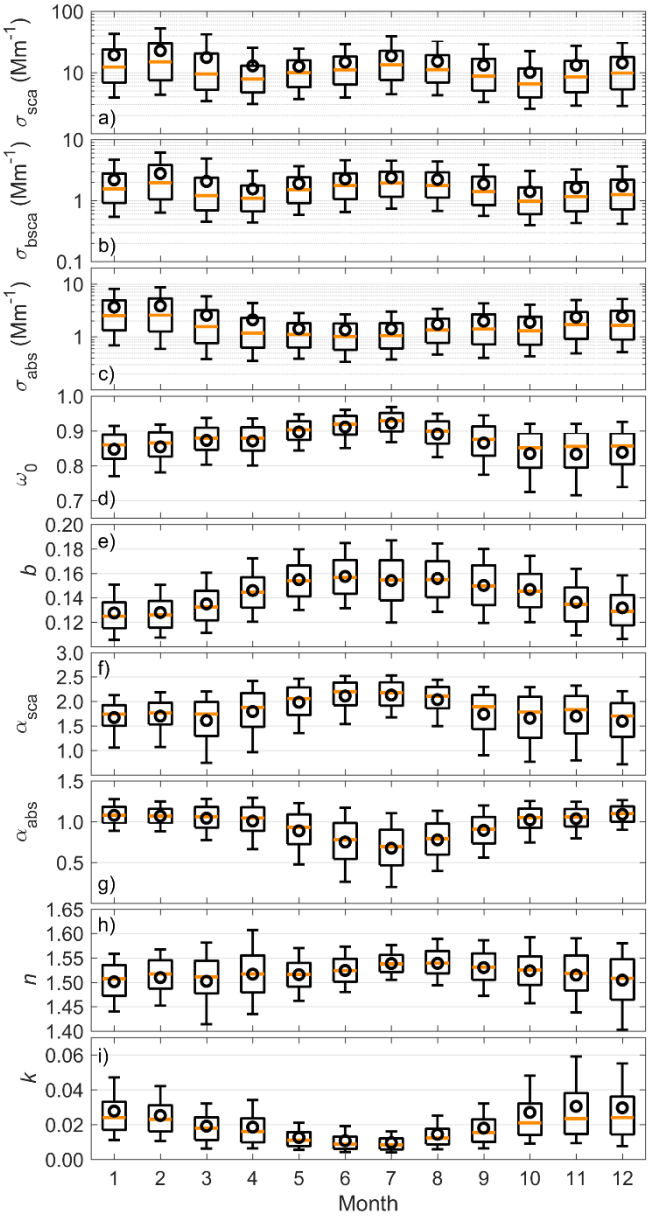

Figure 5: Seasonal variation in the aerosol optical properties for PM10 particles. The boxes represent the 25th and 75th percentiles and the whiskers the 10th and 90th percentiles of the data. The orange line is the median and the mean is presented with a black circle.

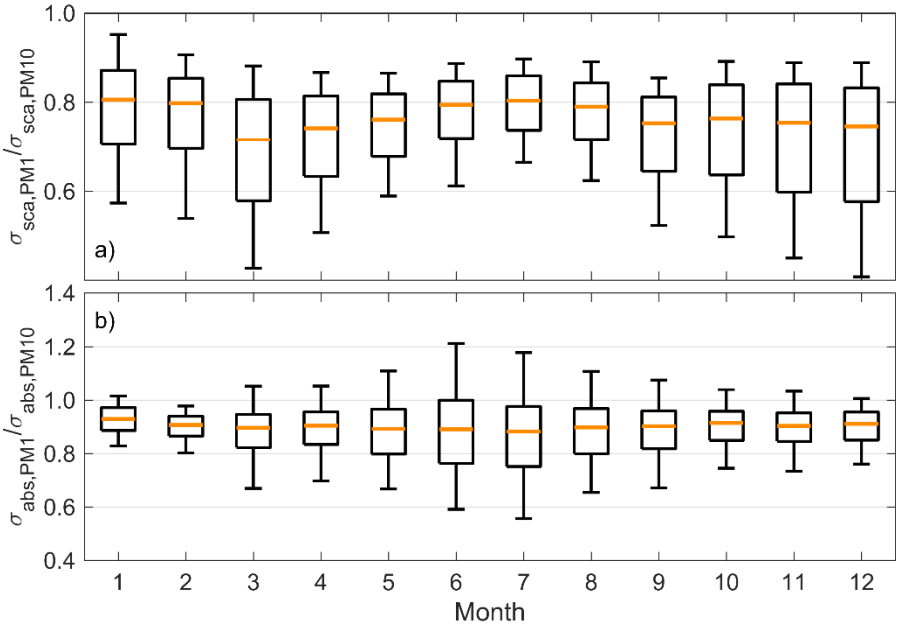

Figure 6: Seasonal variation in the PM1/PM10 ratio for a) σ_{sca} and b) σ_{abs}. The explanation for the boxplots are the same as in Fig. 5.

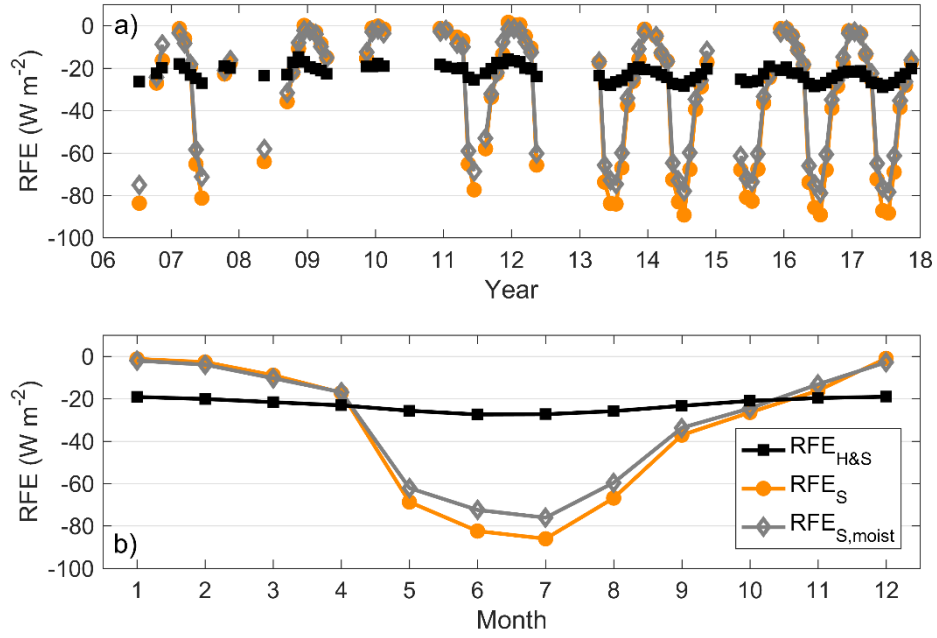

Figure 7: Variations in the different radiative forcing efficiencies at SMEAR II in 2006 – 2018. a) Time series of the $RFE_{H\&S}$, RFE_S, and $RFE_{S,moist}$. The monthly medians are presented if the month had at least 14 days of valid data. b) Seasonal variation of the $RFE_{H\&S}$, RFE_S, and $RFE_{S,moist}$ as overall monthly medians.

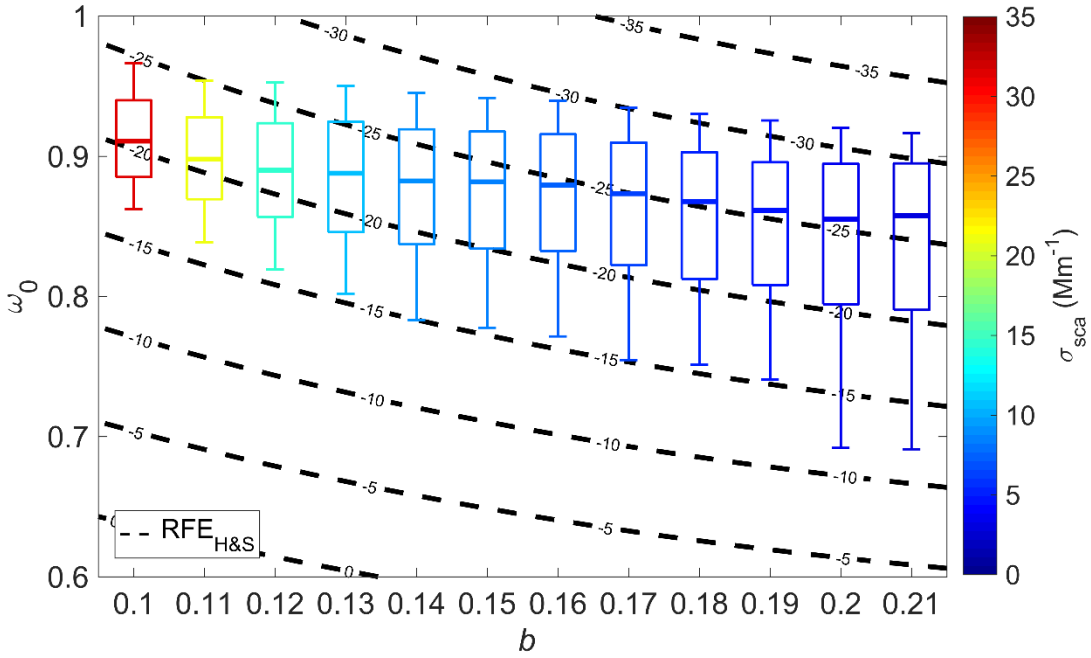

Figure 8: Relationships between ω_0, b and $RFE_{H\&S}$. The $RFE_{H\&S}$ is shown as the dashed isolines in the background. The boxes represent the data measured at SMEAR II and they are colored by the median σ_{sca}. The explanation for the boxplots is the same as in Fig. 5.